Earth Planet. Sci. Lett. 643 (2024) 118923

Contents lists available at ScienceDirect

Earth and Planetary Science Letters

journal homepage: www.elsevier.com/locate/epsl

Crustal-mantle layering deposits in the Von Kármán crater, South Pole-Aitken basin

Zhi Zhong [a,*], Yuqi Qian [b,c], Chenglong Li [a], Alexander Y. Sun [d], Zhongxian Cai [a], Lei Lin [a], Xu Guo [a], Yanbin Kuang [a], Shiqi Wen [a], Long Xiao [c]

[a] *Key Laboratory of Theory and Technology of Petroleum Exploration and Development in Hubei Province, School of Earth Resources, China University of Geosciences, Wuhan, 430074, China*
[b] *Department of Earth Sciences, The University of Hong Kong, Hong Kong, China*
[c] *Planetary Science Institute, School of Earth Sciences, China University of Geosciences, Wuhan, 430074, Hubei, China*
[d] *Bureau of Economic Geology, John A. and Katherine G. Jackson School of Geosciences, The University of Texas at Austin, University Station, Austin, TX, 78713-8924, United States*

ARTICLE INFO

Editor: O. Mousis

Keywords:
Chang'E-4 mission
Lunar penetrating radar
Von Kármán (VK) crater
Data-driven generative deep learning inversion algorithm
Lunar regolith
Shallow stratigraphic structure

ABSTRACT

Comprehending the properties of the Moon's crust and mantle materials is essential for decoding its interior. Whether the South Pole-Aitken (SPA) basin potentially excavated the upper mantle materials remains mysterious. The Chang'E Four Lunar Penetrating Radar (LPR) has provided an unprecedented opportunity to investigate the SPA basin in the Von Kármán (VK) crater. Utilizing a data-driven generative deep learning inversion algorithm, the subsurface physical properties along the Yutu-2 path were determined. 4 distinct deposit zones were discovered beneath the surface. All zones feature an upper low-permittivity (paleo-)regolith layer overlaying on a lower high-permittivity layer of rockier ejecta or basal basalt. Zone 1, an ejecta layer from the Finsen crater within the SPA Compositional Anomaly, has a bulk density ($2.81 \pm 0.22 g/cm^3$) denser than that of highland crust represented by materials originating from VKL and VKL' craters in the Mg-Pyroxene Annulus, which are present in Zones 2 and 3. This suggests the possible presence of mantle materials in Zone 1, providing the first diagnostic evidence that the SPA impact may have penetrated the upper lunar mantle.

1. Introduction

Following the formation of the primary lunar crust through the cooling and solidification of the global lunar magma oceans (Warren, 1985; Lin et al., 2017; Jolliff et al., 2000), the lunar surface has been continuously reshaped by a variety of geological processes, especially impact bombardment and volcanic activities (Hörz et al., 1991; Carrier III et al., 1991). These processes have led to the creation of a complex layering of materials on the lunar surface, including regolith, mega-regolith and volcanic rocks, forming during different periods (Li et al., 2020; Zhang et al., 2020). These materials harbor abundant information about the Moon's inherent and external evolution, with younger stratigraphic units superimposed on older ones.

The South Pole-Aitken (SPA) basin, the largest and most ancient impact basin on the Moon, formed during the pre-Nectarian age period (~ 4.25 Ga) (Fernandes et al., 2013; Garrick-Bethell et al., 2020; Wu et al., 2019). Its formation significantly modified the interior of the SPA basin, and even altered the lunar history by creating the SPA Terrane (Jolliff et al., 2000; Zhang et al., 2022) and may excavate upper mantle materials to lunar surface (Potter et al., 2012; Melosh et al., 2017; Moriarty III et al., 2021). However, there is an ongoing debate regarding the extent to which the formation of the SPA basin resulted in the exposure of upper mantle material. The absence of widespread olivine in the SPA basin has been used to suggest that the mantle has not been exposed by this gigantic impact or obscured by later process (Yamamoto et al., 2012). However, according to numerical impact modeling, even in the most conservative cases, the SPA basin must have sampled the Moon's upper mantle to depths of $100 km$ and inevitably ejected the mantle material onto the farside highlands (Melosh et al., 2017). The discrepancy between different methods urgently needs to be solved by other datasets especially those from geophysical measurements which have the ability to reveal the subsurface properties of the Moon down to the subsurface.

The Von Kármán (VK) crater, situated northwest of the SPA basin, was formed during the pre-Nectarian period. It has an estimated age of $4.2^{+0.03}_{-0.03}$ Ga (Lu et al., 2021) and was formed subsequent to the formation of the SPA basin. The floor of the VK crater is overlain by the

---

* Corresponding author.
E-mail address: zhongzhi@cug.edu.cn (Z. Zhong).

https://doi.org/10.1016/j.epsl.2024.118923
Received 28 February 2024; Received in revised form 26 July 2024; Accepted 29 July 2024

Imbrian-aged basaltic lava flows (Huang et al., 2018) and impact ejecta originating from adjacent impact craters. This has resulted the accumulation of diverse materials (Huang et al., 2018) that chronicle the geological history of the SPA basin. These impact ejecta within VK might originate from adjacent Finsen, Von Kármán L (VKL), Von Kármán L' (VKL') and Antoniadi (Yuan et al., 2021; Huang et al., 2018; Pasckert et al., 2018). However, determining the formation sequence of these impact craters in and around the VK crater poses a challenging task due to the complex impact and post-impact alteration process (Melosh et al., 2017; Cassata et al., 2018; Garrick-Bethell et al., 2010).

A detailed comparison of the terrain surrounding the Finsen and VKL impact craters, using the data from NASA's Gravity Recovery and Interior Laboratory (GRAIL) mission and Lunar Orbiter Laser Altimeter (LOLA), indicates that the Finsen crater formed first and subsequently underwent morphological transformations (Moriarty III et al., 2021; Neumann et al., 2015). In contrast, the VKL impact crater, which exhibits relatively simple features and lacks significantly collapsed floors, ridges, or fissures, possibly formed later (Neumann et al., 2015). Recent Lunar Penetrating Radar (LPR) studies from the Change'E-4 (CE-4) landing site also indicate that the layers of impact ejecta, overlain by the fine regolith layer, are mostly derived from Finsen crater (Lai et al., 2020; Li et al., 2020; Zhang et al., 2021). Additionally, according to Fortezzo et al. (2020), the most probable sequence of impact crater formation, from oldest to youngest, is Maksutov, VKL', VKL, and Finsen, aligning with the aforementioned morphological and LPR results. As such, we have adopted this sequence of impact crater formation in our study.

On January 3^{rd}, 2019, the CE-4 spacecraft carrying the Yutu-2 rover, landed on the VK crater (Fig. 1A). As of July 1^{st}, 2021, the Yutu-2 rover has worked 34 lunar days and traveled ~ 731 meters on the floor of the VK crater (Fig. 1B). The Lunar Penetration Radar onboard the Yutu-2 rover is equipped with two high-frequency channels (CH2A, CH2B 500 MHz) and a low-frequency channel CH1 (60 MHz) (Table S1) to investigate the subsurface structure along its path of travel (Li et al., 2020). The two high-frequency channels have the ability to penetrate a depth of up to 50 m (Li et al., 2020), which is deeper than that was detected by Yutu-1 rover for Chang'E-3 (CE-3), due to the lower $TiO_2 + FeO_2$ content and reduced magnetic loss in the CE-4 landing site (Zhang et al., 2020; Lai et al., 2020; Fa et al., 2015).

Ground Penetrating Radar (GPR) is extensively utilized to characterize shallow subsurface structures from the scale of meters to kilometers, owing to its ability to image subsurface reflectivity (Gao et al., 2023; Wang et al., 2022; Metwaly, 2015; Ciampoli et al., 2016; Al-Nuaimy et al., 2000). As a non-destructive and non-invasive geophysical detection tool (Panda et al., 2022; Comite et al., 2015; Rehman et al., 2016), GPR is also employed in pollution monitoring (Rehman et al., 2016; Peters et al., 1994) and soil moisture content research (Di Matteo et al., 2012; Koyama et al., 2017). All these applications of GPR are directly or indirectly linked to the electromagnetic properties of the object under detection, such as permittivity, electrical conductivity, and magnetic conductivity. Therefore, accurately inverting the electromagnetic properties of the detected object from GPR signals is important for the analysis and interpretation of the detected objects. Hyperbola-fitting methods are the most commonly used technique for GPR data processing. They are also widely applied to invert the underground dielectric properties (Fa et al., 2015; Giannakis et al., 2021; Zhang et al., 2020; Li et al., 2020), aiding in the investigation of the subsurface structure of the VK crater (Lai et al., 2021; Li et al., 2020; Zhang et al., 2021; Dong et al., 2021). However, the origin of these strata is still not well constrained, as these methods may fail to identify several horizons due to the underestimation of dielectric permittivity, as demonstrated by the advanced hyperbola-fitting method (Giannakis et al., 2021; Zhou et al., 2022). The hyperbola-fitting algorithm primarily relies on the principle that individual object buried in the subsurface produces distinct radar reflection features. The pattern of these features is well approximated by a hyperbola or more complicated pattern, depending on the size of the buried object and the properties of the surrounding materials (Giannakis et al., 2021; Li et al., 2020). However, this method is limited to a relatively simple subsurface setting. For example, previous studies used a singular dielectric constant for regolith ($\epsilon = 3$ (Fa et al., 2015) and $\epsilon = 4.3$ (Lai et al., 2020)) to estimate the thickness of subsurface strata. An average dielectric constant ($\epsilon = 3$) (Muhleman et al., 1969), measured in Apollo samples, can also be used if a short stratigraphic interface or homogeneous strata exist on the farside of the Moon. However, as the subsurface structure of the CE-4 landing site is complex and

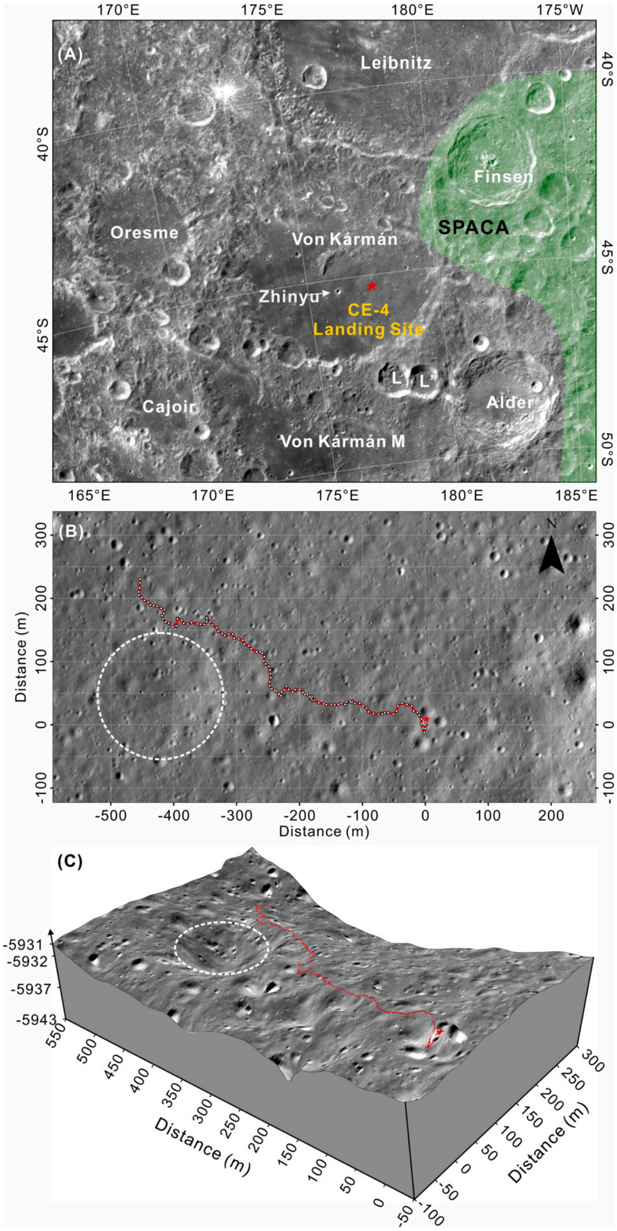

Fig. 1. Chang'E-4 (CE-4) landing site and the traversing path of the Yutu-2 rover during the first 34 lunar days. (A) CE-4 landed on the eastern floor of the Von Kármán crater, marked by a red star (45.4446°S, 177.5991°E) (Liu et al., 2019). The light green area represents the SPA compositional anomaly (SPACA) areawhile the remaining area belongs to the Mg-Pyroxene Annulus area (Moriarty Iii and Pieters, 2018). The image is sourced from a ChangE'2 (CE-2) 20-m resolution digital orthophoto map (Table S2). (B) Traversing the path of the Yutu-2 rover in the first 34 lunar-days. Current cumulative length of the LPR data collection is ~ 731 m. The waypoints (white dots) mark the LPR acquisition locations, and the solid red line indicates the rover's traversing path. The white dotted circle marks the buried crater (Lai et al., 2021). (C) 3D scheme of the landing site. The background image is a high-resolution image from the LROC narrow-angle camera.

the bulk density and material composition vary with the depth and location (Li et al., 2019; Zhang et al., 2020; Feng et al., 2023), it is evidently inappropriate to use a constant dielectric permittivity to describe the dielectric properties of the CE-4 landing site.

With advancements in signal processing studies in recent years, deep learning has been growing rapidly and quickly changing the landscape of various fields, such as natural language processing (Otter et al., 2020), computer vision (LeCun et al., 2004; Goodfellow et al., 2014) and partial differential equation solving (Raissi and Karniadakis, 2018). In this study, we apply a data-driven generative deep learning algorithm to overcome the limitations of hyperbola-fitting methods and to investigate the dielectric permittivity of the lunar subsurface using high-frequency LPR CH2A radar data. This data-driven machine learning algorithm, known as Cycle Generative Adversarial Network (CycleGAN), reformulates the inverse problem as a regression problem and is used to invert the dielectric permittivity of the lunar subsurface structure based on the LPR data transmitted by the Yutu-2 rover. The CycleGAN, derived from adversarial learning, is a type of Generative Adversarial Network (GAN) comprising two competing models (Goodfellow et al., 2014): two pairs of generator and discriminator. The generator attempts to create fake data samples as close to the training data distribution as possible, while the discriminator attempts to distinguish these fake samples from the true ones (Goodfellow et al., 2020). Upon convergence, the discriminator reaches a state of maximum confusion, unable to differentiate between fake and true samples. The adversarial learning capability of GAN enables it to learn data distributions without requiring explicit assumptions from users regarding error distributions (Goodfellow et al., 2015).

Here in this study, a CycleGAN model is well-trained using simulated synthetic radar datasets to quantitatively investigate the dielectric permittivity profile based on the pre-processed radargram. First, we prepared a suite of lunar subsurface geological models according to previous studies (Dong et al., 2020, 2021; Li et al., 2020; Zhang et al., 2020, 2021) and conducted those models using the public gprMax open source code (Warren et al., 2016) to generate numerous synthetic radargram, which not only solves the problem of the insufficient training dataset but also introduces the physics-based principles into the learning process. In generating the synthetic training dataset, various scenarios were considered, such as systematically varying permittivity values. Moreover, the soil fractal algorithm increases the variability of permittivity values in the horizontal direction. The final testing performance shows that the well-trained CycleGAN model can invert the permittivity with high accuracy, such that the subsurface geological model and the inverted permittivity profile only have minor errors. Then, we use the well-trained CycleGAN model to invert the 2D electric permittivity profile of the LPR CH2A dataset in the time domain along the traveling path of the Yutu-2 rover. The permittivity profile is converted from time to depth domain, in which the permittivity is not monotonously increased from top to bottom; instead, it changes along the depth and is in the range of 2 ∼ 7 from top to bottom. Our results are consistent with a recent study by Giannakis et al. (2021), who applied a more advanced hyperbola-fitting algorithm to check the accuracy of the inferred permittivity profile.

In this study, a CycleGAN model is well-trained using simulated synthetic radar datasets to quantitatively investigate the dielectric permittivity profile based on the pre-processed radargram. Initially, we prepared a suite of lunar subsurface geological models according to previous studies (Dong et al., 2020, 2021; Li et al., 2020; Zhang et al., 2020, 2021) and used the public gprMax open-source code (Warren et al., 2016) to generate numerous synthetic radargrams. This approach not only addresses the issue of insufficient training data but also integrates physical principles into the learning process. In generating the synthetic training dataset, various scenarios were considered, such as systematically varying permittivity values. Moreover, the soil fractal algorithm was employed to increase the variability of permittivity values in the horizontal direction. The final testing performance demonstrates that the well-trained CycleGAN model can accurately invert the permittivity, with minor errors between the subsurface geological model and the inverted permittivity profile. Then, the well-trained CycleGAN model is applied to invert the 2D electric permittivity profile of the LPR CH2A dataset in the time domain along the Yutu-2 rover's travel path. The permittivity profile was converted from the time to depth domain, revealing that permittivity does not increase monotonically from top to bottom. Instead, it fluctuates along the depth and ranges between 2 and 7 from the top to the bottom. Our results align with a recent study by Giannakis et al. (2021), who employed a more advanced hyperbola-fitting algorithm to verify the accuracy of the inferred permittivity profile.

2. Methodology

2.1. Lunar penetrating radar (LPR) data processing

Reflexw is a popular and reliable geophysical near-surface processing and interpretation package (Sandmeier, 2023), which was used to process LPR data as follows.

(1) Effective data extraction. Since Yutu-2 rover still continues radar data acquisition even during pauses for route planning or the collection of other scientific data, numerous duplicate entries exist in the radar profile. To eliminate the discontinuities of radar data, 20247 traces of CH2A data have been manually extracted through visual determination, following the process workflow (Zhang et al., 2020).

(2) Direct current (DC) removal. To restore the signal to its true amplitude, it is necessary to remove the low-frequency component with a frequency close to DC. We processed the extracted data by employing the subtract-mean (dewow) function in Reflexw, using a time window of 10 ns.

(3) Static correction/First arrival removal/Time zero correction. Given that the receiver is triggered prior to the source, it is necessary to adjust for this time difference. The "move starttime" method in Reflexw has been applied to remove 28.203 ns signals from the top of the CH2A data, thus preventing a time delay (Zhang et al., 2020).

(4) Amplitude compensation. Due to energy absorption, the deep signal is weaker than the shallow signal. Therefore, the deep signal requires spherical spreading correction and amplitude compensation via gain based on the wave propagation distance. For this purpose, the energy decay gain method in Reflexw was applied.

(5) Filter processing. In order to reduce interference at high and low frequencies and enhance the signal-to-noise ratio of the data, we employed the "bandpass" operation in Reflexw to filter the CH2A data. The filtering parameters, which include a lower cut-off, lower plateau, upper plateau, and upper cut-off, are set at 100 MHz, 250 MHz, 750 MHz, and 900 MHz, respectively.

(6) Background removal. Given the significant horizontal noise present in the CH2A data, background removal operation is applied to the CH2A data starting from 50 ns to prevent impacts on the shallow horizontal strata.

(7) Resampling. Since the time cost of synthesizing the data is too high, the sampling interval of the synthesized data has been set to 0.15625 ns to meet the requirement of the input data length of the neural network, and it is also necessary to resample the data of Channel-2A to the same sampling frequency.

2.2. Inverse problem

Traditionally, the inverse problem (Qin et al., 2023) for ground penetrating radar (GPR) can be formed as follows:

$$\Phi(\mathbf{m}) = \Phi(\mathbf{u}) = \frac{1}{2}||\mathcal{R}\mathbf{u}(\mathbf{m}) - \mathbf{d}^{obs}||_2^2 = \frac{1}{2}||\Delta\mathbf{d}||_2^2 \tag{1}$$

where the Φ is the objective function, $\mathbf{u}$ is the synthetic wave field at the receiver position by the restriction operator $\mathcal{R}$, $\mathbf{m}$ is the model parameters, and $\Delta\mathbf{d} = \mathcal{R}\mathbf{u}(\mathbf{m}) - \mathbf{d}^{obs}$ is the residual between the forward simulation data $\mathcal{R}\mathbf{u}(\mathbf{m})$ and the observed data $\mathbf{d}^{obs}$. Conventionally, one achieves an optimal subsurface image by minimizing the difference between the observed and the synthetic waveforms. Therefore, the ultimate purpose of solving the inversion problem is to seek the most appropriate model parameters $\mathbf{m}$, which can minimize the objective function Φ as follows:

$$\begin{aligned}\mathbf{m}^* &= \underset{m}{\operatorname{argmin}}\, \Phi(\mathbf{m}) \\ &= \underset{m}{\operatorname{argmin}}\, \frac{1}{2}\|\mathcal{R}\mathbf{u}(\mathbf{m}) - \mathbf{d}^{obs}\|_2^2\end{aligned} \tag{2}$$

However, the complexity of the subsurface, including geological structures, subsurface material properties, and boundary conditions, introduces significant uncertainties and non-uniqueness into the inversion process. This makes it challenging to accurately reconstruct the subsurface properties (Qin et al., 2023). Furthermore, geophysical inversion is a nonlinear problem that is difficult to solve using traditional linear methods. Nonlinearities in the inversion process can lead to non-unique solutions and make it challenging to determine the most likely subsurface model (Giannakis et al., 2021). The sparse and noisy nature of geophysical data also impacts the quality and reliability of the inversion results (Fa et al., 2015). By addressing the complexities arising from the intricate subsurface structure, nonlinearity of the inversion problem, incomplete data, and parameter coupling, researchers can strive to develop more robust and reliable inversion methods, which would be capable of accurately imaging and characterizing the subsurface properties of the geobody.

2.3. gprMax3D synthetic dataset

In order to invert the dielectric permittivity using neural networks, a large volume of labeled data is needed to train the neural network model. However, as the dielectric permittivity profile corresponding to the radar signals is unavailable in actual detection, training and validation data can only be obtained by running forward numerical simulations. Furthermore, gprMax3D, an open-source software that models electromagnetic wave propagation in the subsurface using the finite-difference time-domain (FTDT) method (Warren et al., 2016), requires extensive computational resources in terms of processing time. Consequently, a CUDA-based graphics processing unit (GPU) acceleration engine for gprMax3D (Warren et al., 2019) was developed to enhance computational efficiency, achieving a speed more than 30 times faster than multi-core central processing units (CPUs) using OpenMP parallelization (Koyan and Tronicke, 2020). In this study, GPU-accelerated gprMAX3D v.3.1.4 software has been applied to generate numerous 2D LPR signals using our synthetic geological subsurface models (Warren et al., 2019). To account for possible trends in the permittivity, the workflow for gprMax3D to generate synthetic datasets includes the following steps.

(1) **Lunar subsurface geological models:** As mentioned before, the travel route of the Yutu-2 rover is not a straight line (1B), and the trace distances between adjacent LPR traces are not strictly equal due to temporary pauses and repeated collection. Therefore, it is more reasonable to invert the LPR data trace by trace instead of as a 2D profile. Based on this analysis and to maintain a balance between the gprMax source code computation efficiency and geological model variability, our space-filling design involves two types of geometric models filled with 10 types of geological property models (Fig. 2). The geometry of the 2D geological model includes (1) a geometric model with dimensions of 12.5 m ×21.0 m in the vertical (z) and horizontal (x) directions (Fig. 2a-h), and (2) a geometric model with dimensions of 0.9×12.5 m in the vertical (z) and horizontal (x) directions (Fig. 2i, j). Both geometry models have the same cell size of 0.005 m ($\Delta x = 0.005$ m, $\Delta z = 0.005$ m) in the vertical (z) and horizontal (x) directions. Previous studies have indicated that the dielectric permittivity of the lunar subsurface increases from the regolith to the bottom layers (Li et al., 2020) or changes from the top to the bottom layers (Lai et al., 2021; Giannakis et al., 2021). Therefore, we designed 10 types of geological property models to fill the geometric models. As listed in Table S2, different geological models utilize different geometric models. To emphasize the layering of the lunar subsurface, we designed multiple layers in different geological models, with the number of layers varying from 1 to 10. Each layer is either homogeneous with a constant dielectric permittivity ranging from 2 to 10 (Table S1 Type 1), or heterogeneous with values generated via the FractalVolume function (Giannakis et al., 2016). In the latter case, the number of materials for each model randomly changes from 20 to 200, and up to 500 in several types, and the dielectric permittivity for each material randomly changes from 2 to 10 (Table S2 Types 2-8). Additionally, to align with the interpretation results in Li et al. (2020); Zhang et al. (2020) and increase the diversity of the training dataset, we also randomly added rocks with diameters ranging from 0.001 m to 0.005 m. The number of rocks increases from the left to right side (Fig. 2a and b). Finally, we uniformly sample 500 random numbers in the range of $[2, 10]$ and assign them to each of the 500 materials as dielectric constants in the order of the values (Fig. 2i,j). All the model types and geometry types are provided in Table S3.

(2) Data simulation. Then, gprMax v.3.1.4 (Warren et al., 2016) was used to carry out extensive 2D GPR modeling using the generated lunar subsurface geological models, with the simulation parameters listed in Table S2. The computation time was dependent on the number of cells in a model domain. The GPU version of gprMAX3D v.3.1.4 software (Warren et al., 2019) has been applied to speed up the simulation process. Additionally, several other Python package dependencies, including pycuda (https://pypi.org/project/pycuda/) and mpi4py (https://pypi.org/project/mpi4py/0.4.0/), were also installed. Each geological model was loaded onto a single NVIDIA GPU (V100, 32G) to perform the numerical simulation. One complete simulation task, comprising a total of 4200 traces of the type 1 geological model (Table S1), required approximately 4.5 hours. This demonstrates that the forward numerical simulation of radar wave propagation is both time-consuming and the most challenging aspect of using traditional methods for inversion, such as Full Waveform Inversion (FWI). As the Yutu-2 rover continuously moves and sends the LPR dataset to Earth, using FWI to invert the LPR data becomes increasingly difficult. Fig. 3a shows one lunar subsurface geological model, and Figs. 3b-g show the wave propagation at different time points.

(3) Data processing. The synthesized data need to undergo processing similar to that used for LPR data, including DC removal, time-zero correction, amplitude compensation, and filter processing. Fig. 3 h-k illustrate the processed results of the simulated trace at various processing stages, while Fig. 3 l presents the final processed synthetic radargram, which serves as the ultimate training dataset in CycleGAN.

(4) Dataset delineation and normalization. After the synthetic radar data are processed, they are randomly split into 80%, 10%, and 10% for the training, validation, and testing datasets, respectively. Additionally, each trace is selected with a length of 1024, with a random length to maintain variability.

2.4. Cycle-generative adversarial neural network (CycleGAN)

The CycleGAN consists of two pairs of generators and discriminators. In our case, the first pair of the generator (G_{x-y}) and discriminator (D_{x-y}) is responsible for inferring the permittivity, using the radar signal as input and permittivity as output. The second pair of generators (G_{y-x}) and discriminators (D_{y-x}) tasked with reconstructing the radar signals from the inverted permittivity. The CycleGAN network structure facilitates the inversion of lunar subsurface properties from the high-frequency radar signal domain using a limited dataset (Fig. 4).

(1) The workflow and architecture of CycleGAN. CycleGAN used in this study is a variant of the original GAN, which integrates the forward and backward process in one framework and is suitable for cross-domain learning (Zhu et al., 2017). Specifically, CycleGAN con-

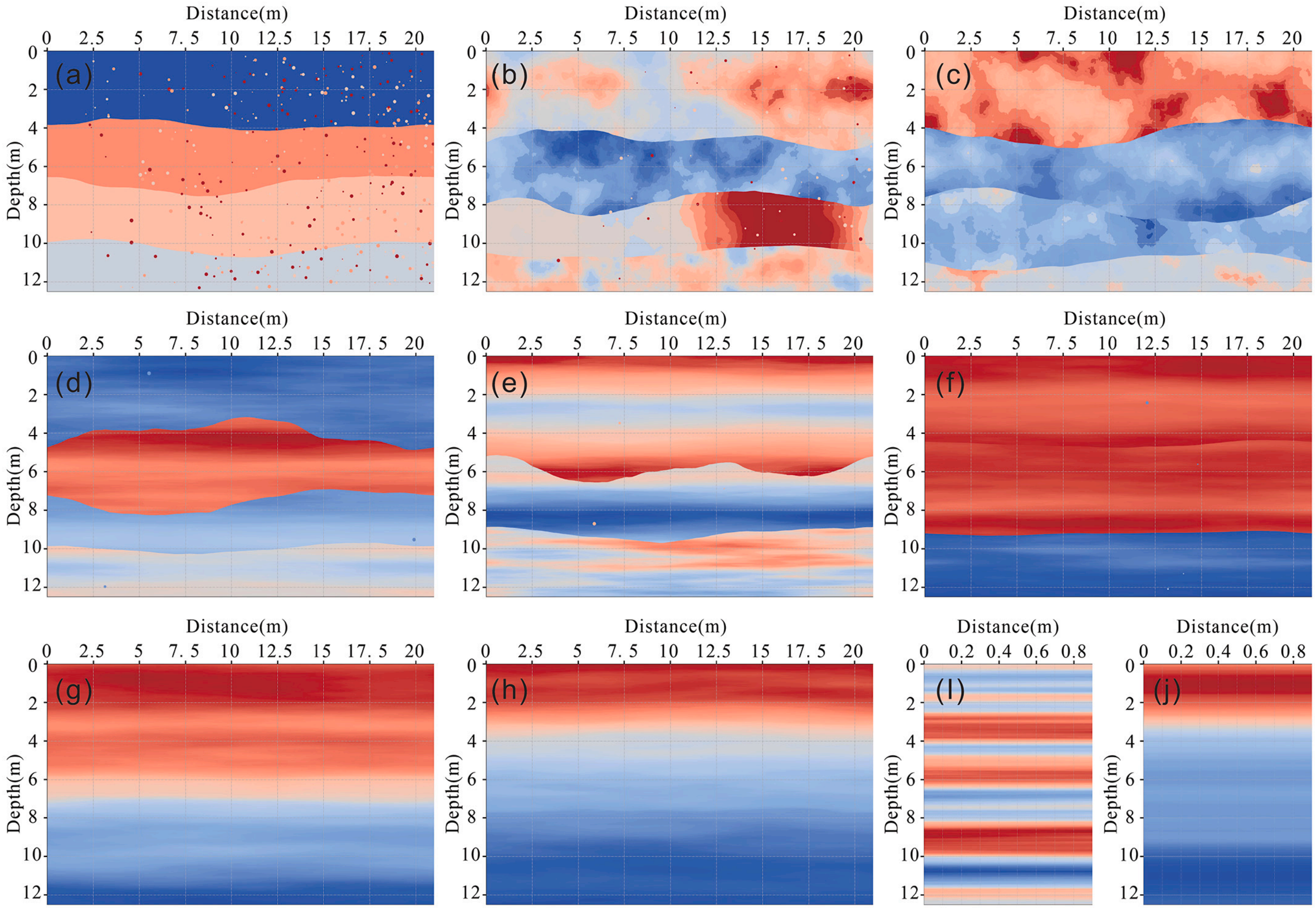

Fig. 2. Synthetic lunar subsurface geological model types. Ten types of subsurface lunar geological models. (a) type 1: Size 21 m × 12.5 m number of layers from 1 to 10, uniform layers, 13 materials, large number of stones, dielectric constant in the range of $[2, 10]$, completely random in the longitudinal direction, (b) type 2: Size 21 m × 12.5 m, number of layers from 1 to 10, intra-layer fractal, number of materials from 20 to 200, small number of rocks, median dielectric constant (ε_m) of each layer chosen randomly from 2 to 10, dielectric constant range $[\varepsilon_m - 2, \varepsilon_m + 2]$, completely random in the longitudinal direction, (c) type 3: Size 21 m × 12.5 m, number of layers from 1 to 10, fractal within layers, number of materials from 20 to 200, no stones, median dielectric constant (ε_m) of each layer chosen randomly from 2 to 10, dielectric constant range $[\varepsilon_m - 2, \varepsilon_m + 2]$, completely random in the longitudinal direction, (d) type 4: Size 21 m × 12.5 m, number of layers from 1 to 10, intra-layer fractal, 500 materials, few stones, median dielectric constant (ε_m) of each layer chosen randomly from 2 to 10, dielectric constant range $[\varepsilon_m - 0.5, \varepsilon_m + 0.5]$, completely random in the longitudinal direction, (e) type 5: Size 21 m × 12.5 m, number of layers from 1 to 5, intra-layer fractal, 500 materials, few stones, median dielectric constant (ε_m) of each layer chosen randomly from 2 to 10, dielectric constant range $[\varepsilon_m - 0.5, \varepsilon_m + 0.5]$, completely random in the longitudinal direction, (f) type 6: Size 21 m × 12.5 m, number of layers from 1 to 10, intra-layer fractal, 500 materials, no stones, median dielectric constant (ε_m) of each layer chosen randomly from 2 to 10, dielectric constant range $[\varepsilon_m - 0.5, \varepsilon_m + 0.5]$, completely random in the longitudinal direction, (g) type 7: Size 21 m × 12.5 m, integral fractal, material type from 400 to 500, no stone, median dielectric constant (ε_m) chosen randomly from 2 to 10, dielectric constant taken in the range of $[\varepsilon_m - 0.5, \varepsilon_m + 0.5]$, increasing in the longitudinal direction, (h) type 8: Size 21 m × 12.5 m, integral fractal, material type from 400 to 500, no stone, dielectric constant takes values in the range $[2, 10]$, increasing in the longitudinal direction, (i) type 9: Size 0.9 m × 12.5 m, overall fractal, material type from 400 to 500, no stone, dielectric constant taking values in the range $[2, 10]$, completely random in the longitudinal plane, (j) type 10: Size 0.9 m × 12.5 m, integral fractal, material type from 400 to 500, no stone, dielectric constant takes values in the range $[2, 10]$, increasing in the longitudinal direction.

sists of two pairs of GANs: $(\mathcal{G}_{X\rightarrow Y}, \mathcal{D}_Y)$ and $(\mathcal{G}_{Y\rightarrow X}, \mathcal{D}_X)$ (Fig. 4a). The generator $\mathcal{G}_{X\rightarrow Y}$ is responsible for transforming Domain X (radar signal) to Domain Y (dielectric permittivity), and the other generator $\mathcal{G}_{Y\rightarrow X}$ is responsible for transforming Domain Y (dielectric permittivity) back to Domain X (radar signal). $\mathcal{D}_Y$ determines the probability of a sample (y) coming from $\mathcal{G}_{X\rightarrow Y}$ or from the original dataset $DataY$ (Zhong et al., 2020). Similarly, $\mathcal{D}_X$ provides the probability of a sample (x) coming from $\mathcal{G}_{Y\rightarrow X}$ or from the original dataset $DataX$ (Fig. 4b). The loss function of CycleGAN includes three terms: the adversarial loss for each generator/discriminator pair (Goodfellow et al., 2015) and a cycle consistency loss (Zhu et al., 2017),

$$\begin{aligned}\mathcal{L}(\mathcal{G}_{X\rightarrow Y}, \mathcal{G}_{Y\rightarrow X}, \mathcal{D}_X, \mathcal{D}_Y) =& \mathcal{L}_{GAN}(\mathcal{G}_{X\rightarrow Y}, \mathcal{D}_Y, X, Y)\\ &+\mathcal{L}_{GAN}(\mathcal{G}_{Y\rightarrow X}, \mathcal{D}_X, Y, X)\\ &+\mathcal{L}_{cyc}(\mathcal{G}_{X\rightarrow Y}, \mathcal{G}_{Y\rightarrow X}),\end{aligned}$$

where

$$\begin{aligned}\mathcal{L}_{GAN}(\mathcal{G}_{X\rightarrow Y}, \mathcal{D}_Y, X, Y) =& \mathbb{E}_{y\sim p^Y_{data}(y)}[\log \mathcal{D}_Y(y)]\\ &+\mathbb{E}_{x\sim p^X_{data}(x)}[\log(1-\mathcal{D}_Y(\mathcal{G}_{X\rightarrow Y}(x))],\\ \mathcal{L}_{GAN}(\mathcal{G}_{Y\rightarrow X}, \mathcal{D}_X, Y, X) =& \mathbb{E}_{x\sim p^X_{data}(x)}[\log \mathcal{D}_X(x)]\\ &+\mathbb{E}_{y\sim p^Y_{data}(y)}[\log(1-\mathcal{D}_X(\mathcal{G}_{Y\rightarrow X}(y))],\\ \mathcal{L}_{cyc}(\mathcal{G}_{X\rightarrow Y}, \mathcal{G}_{Y\rightarrow X}) =& \mathbb{E}_{x\sim p^X_{data}(x)}[\|\mathcal{G}_{Y\rightarrow X}(\mathcal{G}_{X\rightarrow Y}(x)) - x\|_1]\\ &+\mathbb{E}_{y\sim p^Y_{data}(y)}[\|\mathcal{G}_{X\rightarrow Y}(\mathcal{G}_{Y\rightarrow X}(y)) - y\|_1].\end{aligned}$$

where $\mathbb{E}$ is the expectation operator. The parameters of CycleGAN ($\hat{\theta}$) can be obtained by solving the following minimax problem:

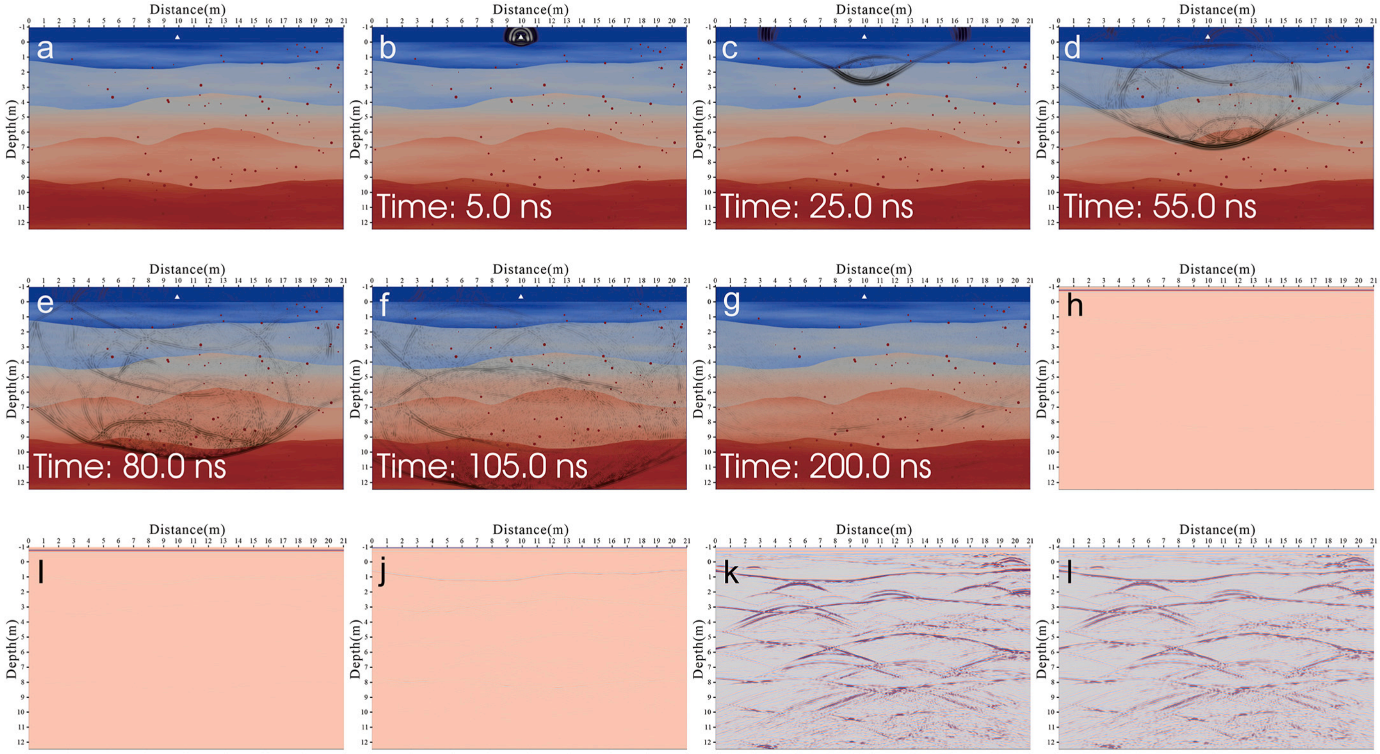

Fig. 3. Numerical simulation result of synthetic lunar subsurface geological model. (a) the lunar subsurface geological model has a horizontal distance of 21 m and vertical depth of 12.5 m, respectively, with a cell size of $0.005m$ in the x and z directions. The white triangle marks one location of LPR. The distance between the transmitter and surface is set as $30cm$ in these models, consistent with the LPR equipment on Yutu-2 Rover (Li et al., 2020), (b)-(g) the wave propagation snapshots at the time points of $5.0ns$, $25.0ns$, $55.0ns$, $80.0ns$, $105.0ns$ and $200.0ns$ using open source code gprMax (Warren et al., 2016), respectively. It can be seen that the shape of the electric-magnetism wave is different at different time points. It should be noted that the time window in this mode is $200ns$ to accelerate the simulation time while retaining the most significant radar information, as the radar signals are weak and require extended numerical calculations. In contrast, the time window of LPR CH2A is $640ns$. (h) the simulated radar game of the synthetic lunar subsurface geological model before the data process, (i) the radargram after Direct-current (DC) removal, (j) the radargram after Static correction/first arrival removal/Time zero correction, (k) the radargram after Amplitude compensation, (l) the radargram after Filter processing.

$$\begin{aligned}&\hat{\theta}^{(\mathcal{G}_{X\to Y})}, \hat{\theta}^{(\mathcal{G}_{Y\to X})}, \hat{\theta}^{(\mathcal{D}_X)}, \hat{\theta}^{(\mathcal{D}_Y)},\\ &= \arg \min_{\theta^{(\mathcal{G}_{X\to Y})}, \theta^{(\mathcal{G}_{Y\to X})}} \max_{\theta^{(\mathcal{D}_X)}, \theta^{(\mathcal{D}_Y)}} \mathcal{L}(\mathcal{G}_{X\to Y}, \mathcal{G}_{Y\to X}, \mathcal{D}_X, \mathcal{D}_Y),\end{aligned} \tag{3}$$

(2) Training and Testing CycleGAN. In this training process, a total of 1.86×10^5 traces are generated using the gprMax software and are employed to train the CycleGAN model. The Adam optimizer is applied to enhance convergence. Two metrics are used to quantify the performance of CycleGAN. The root square mean error (RMSE) is the most commonly used performance metric and is defined as $RMSE = \sqrt{\frac{1}{N}\sum_{i=1}^{N} \|\mathbf{x}^i - \hat{\mathbf{x}}^i\|_2^2}$. The coefficient of determination (R^2) is another metric used to measure the closeness between two variables, which is defined by $R^2 = 1 - \frac{\sum_{i=1}^{N}(\mathbf{x}^i - \hat{\mathbf{x}}^i)}{\sum_{i=1}^{N}(\mathbf{x}^i - \bar{\mathbf{x}})}$, where N is the number of samples, $\mathbf{x}^i$ and $\hat{\mathbf{x}}$ are the true and CycleGAN-predicted results, and $\bar{\mathbf{x}}$ is the average value of the true image.

3. Results

3.1. Validation on synthetic data

An example of using well-trained CycleGAN to invert the permittivity on synthetic data is shown in Fig. 5. Fig. 5a displays the synthetic radar signal after general data processing and normalization, Fig. 5b presents the corresponding normalized geological permittivity model, Fig. 5c shows the permittivity obtained from inversion using CycleGAN, while Fig. 5d displays the result after applying Gaussian filtering to Fig. 5c. Fig. 5e illustrates the error between the inverted permittivity (Fig. 5c) and the true permittivity (Fig. 5b). Statistical analysis of the errors indicates that these are generally within the range of $[0.0, 0.25]$. Further analysis was conducted by extracting two traces from the inversion result, as depicted in Figs. 5g-j. For Trace #290, the R^2 and $rmse$ values between the true permittivity and CycleGAN-predicted permittivity are 0.95 and 0.06, respectively. For Trace #82, the R^2 and $rmse$ values between the true permittivity and CycleGAN-predicted permittivity are 0.93 and 0.07, respectively. In comparison, the R^2 and $rmse$ of between the true permittivity and CNN-predicted permittivity are 0.85 and 0.10 for Trace #290, and are 0.86 and 0.11 for Trace #82, respectively. Based on these analysis results, we believe that the trained CycleGAN is able to invert the permittivity from the ground-penetrating radar signals with high accuracy. Consequently, the subsurface geological model (Fig. 5 b) and the inverted permittivity profile (Fig. 5c) exhibit only minor discrepancies (Fig. 5e and 5f). Therefore, we applied it to the Lunar Penetrating Radar dataset collected by Yutu-2 rover.

3.2. Dielectric permittivity inversion from LPR CH2A

We processed the LPR CH2A high-frequency LPR data and the radar reflection profile using the same radar data processing workflow as proposed by (Lai et al., 2021; Zhang et al., 2020), which includes preprocessing, background removal, gain, and bandpass filtering. The resulting radar profile in the time domain (Fig. 6A), corresponding to the Yutu-2 rover's travel path, shows time-varying reflection characteristics from top to bottom, with several subsurface reflection features similar to those proposed and illustrated in previous studies (Li et al., 2020; Zhang et al., 2021; Yuan et al., 2021; Zhang et al., 2020; Lai et al., 2020). The permittivity profile is then transformed from the time to depth domain (Fig. 6B). Interestingly, the permittivity does not display a monotonic

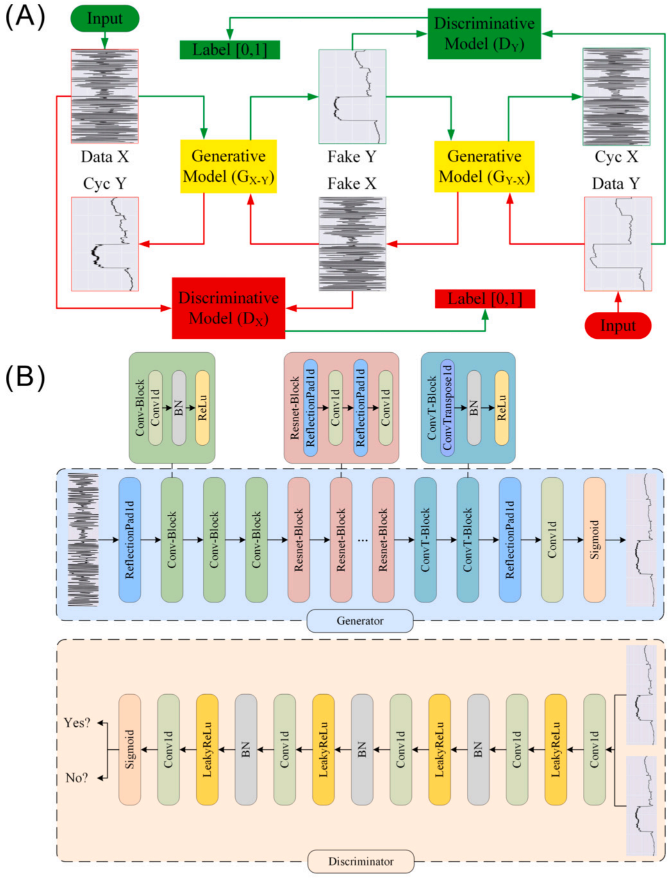

Fig. 4. The workflow and architecture of CycleGAN. (A) The general workflow of CycleGAN. The CycleGAN has two flows: the forward flow and the backward flow. The forward flow, represented by solid green lines, mimics the property inversion process. The backward flow, marked by solid red lines, mimics the numerical simulation process using gprMax open-source code (Warren et al., 2016). In the forward flow, radar signals ($DataX$) are input into the generative model ($\mathcal{G}_{X\rightarrow Y}$) to obtain the output permittivity ($FakeY$). To ensure that the predicted permittivity ($FakeY$) can be inverted back to the radar signal domain ($CycX$), $FakeY$ is input into the generative model ($\mathcal{G}_{X\rightarrow Y}$) to obtain the recycled output permittivity ($CycX$). The primary purpose of the forward flow is to ensure that $DataX$ (radar signal domain) can be transformed into $FakeY$ (permittivity domain) and then reverted to $DataX$ (radar signal domain). The discriminator (D_Y) determines whether the predicted permittivity ($FakeY$) is the same or close to the real permittivity ($DataY$). In the backward flow, the permittivity ($DataY$) is input into the generative model ($\mathcal{G}_{Y\rightarrow X}$) to obtain output radar signals ($FakeX$). The generative model ($\mathcal{G}_{Y\rightarrow X}$) then transformed the radar signals ($FakeX$) into permittivity ($CycY$). The discriminator model (D_X) determines the probability of the generated $FakeX$ belonging to the real permittivity distribution. (B) The CycleGAN framework comprises a pair of identical generators and a pair of identical discriminators, which collectively contribute to the effective functioning of the architecture. Additionally, to demonstrate the advances of CycleGAN in the field of geophysical inversion, a Convolutional Neural Network (CNN) is also employed, which shares the same architecture as the generator of CycleGAN.

increase from top to bottom. In contrast, it varies with depth and ranges between 3.5 ∼ 6.5. To validate the accuracy of the inferred permittivity profile depicted in Fig. 6A, a forward numerical simulation using convolution calculations (Lai et al., 2021) has been conducted. The simulation results confirm that the inferred permittivity is physically plausible (Fig. S1 and S2).

3.3. Wave velocity and density

Wave velocity is the critical bridge between depth and time. After the dielectric permittivity profile of the lunar subsurface is inverted (Fig. 6B), the wave velocity model can be derived using the following equation, which is based on the permittivity profile in homogeneous media:

$$v = \frac{c}{\sqrt{\epsilon_r}} \tag{4}$$

where $c = 299,792,458\ m/s$ is the speed of light in vacuum, and ϵ_r is the relative dielectric permittivity, which is inverted by the CycleGAN in this study. The estimated wave velocity for the upper lunar regolith is approximately to 0.15 m/ns, which aligns with prior findings that employed the hyperbola-fitting algorithm (0.16 m/ns) (Li et al., 2020; Lai et al., 2021). Nonetheless, it is important to note that the wave velocity exhibits variations from the top to the bottom. Several high-velocity zones might be interpreted as components of the weathered regolith layer (Fig. 6C), which will be further examined in the Discussion section. As Fig. 6B displayed, these high-velocity zones are not constant horizontally, contrary to the proposition made in Li et al. (2020). Therefore, a more reasonable explanation is necessary to describe these phenomena. The variations in wave velocity and the presence of high-velocity zones within the lunar regolith suggest complex subsurface structures and compositions that differ from previous assumptions. These variations could be attributed to factors such as differences in material composition, grain size, porosity, and the presence of buried rocks or voids. A thorough investigation into the geological and physical properties of these high-velocity zones is essential to understand their formation and distribution. Future studies should focus on integrating additional data sources, such as seismic surveys and in-situ measurements, to provide a comprehensive understanding of the subsurface characteristics. This will enhance the accuracy of the permittivity and wave velocity models and offer deeper insights into the geological processes shaping the lunar regolith.

Previous laboratory measurements indicate that the wave velocity depends on the material bulk density (Li et al., 2020; Zhang et al., 2020), the bulk density of the lunar subsurface can be estimated by the following formula proposed by Olhoeft and Strangway (1975):

$$\rho = \frac{log(\epsilon_r)}{log(1.92)} \tag{5}$$

and the equation proposed by Hickson et al. (2018):

$$\rho = \frac{(\frac{c}{v})^{(\frac{2}{3})} - 1}{0.307} \tag{6}$$

to calculate the density at different depths (Fig. 8). The bulk density, as illustrated in Fig. 8, was calculated utilizing the wave velocity and dielectric permittivity profile (Fig. 6B). The bulk density profile exhibits a pattern similar to the dielectric permittivity profile. Based on the calculation, the bulk densities of top layer are $2.63 \pm 0.29\ g/cm^3$ (by Eq. (5)), and $2.58 \pm 0.35\ g/cm^3$ (by Eq. (6)). As depicted in Fig. 8, the calculated density, based Olhoeft's model and Hickson's model (Fig. 8), shows various changes along the Yutu-2 rover traveling path and also exhibits variation from top to bottom within the range of 1.45 g/cm^3 to 3.2 g/cm^3 vertically, resulting in values that diverge from the previously calculated values of $1.67 \pm 0.07\ g/cm^3$ and $1.90 \pm 0.08\ g/cm^3$, as reported by Li et al. (2020). Moreover, the density profile calculated based on Olhoeft's model (Fig. 8A) is systematically greater than that calculated based on Hicksons's model (Fig. 8B). The densities near the lunar subsurface are close to 2.35 g/cm^3 and 2.19 g/cm^3, respectively. However, previous research indicated that the bulk density gradually increases with the depth (Dong et al., 2020) or significantly changes at a depth of $\leq$ 1 m (Lai et al., 2020), or it remains constant at approximately 1.76g/cm^3 (Carrier III et al., 1991).

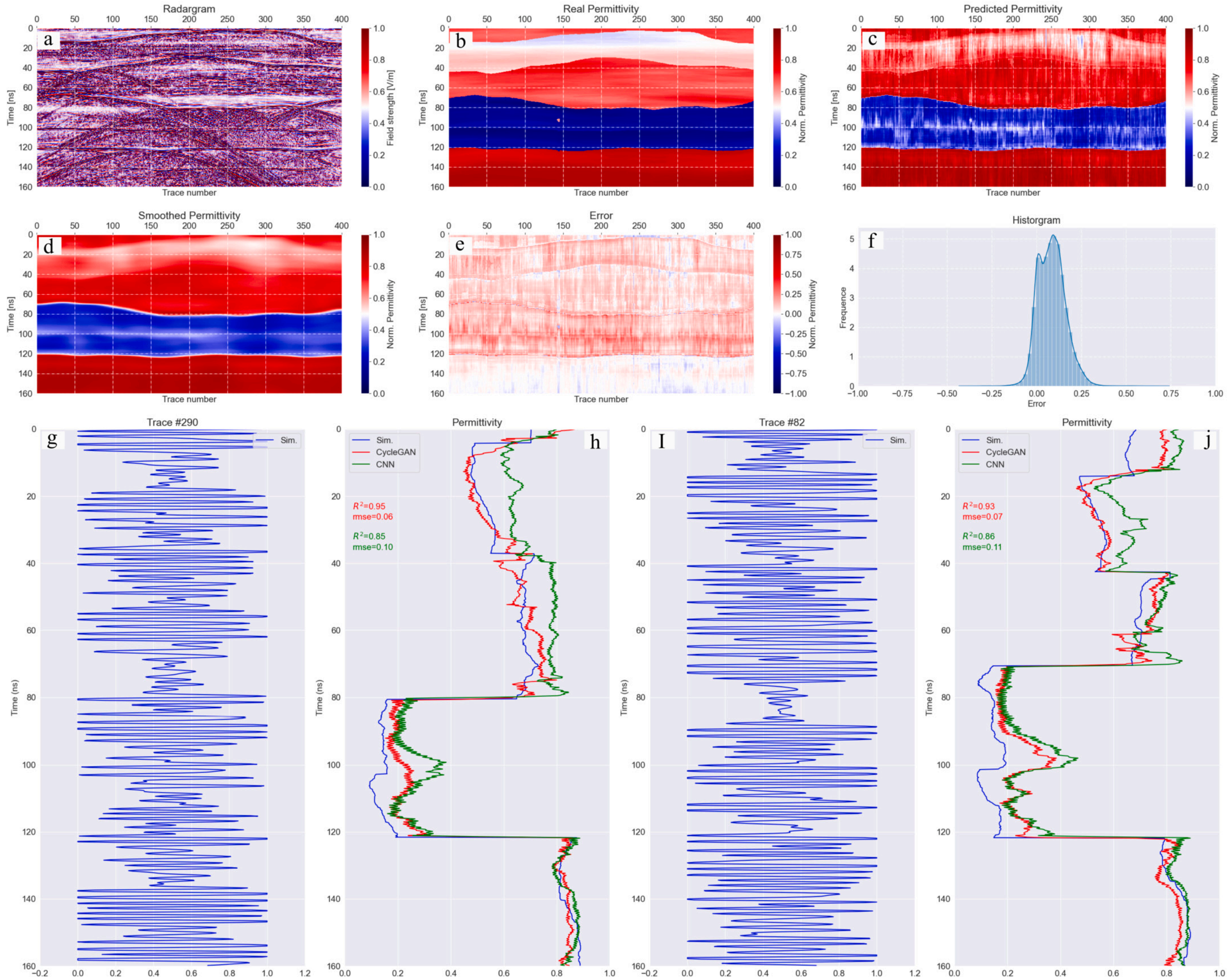

Fig. 5. Synthetic lunar subsurface geological model and corresponding radargram. (a)the normalized radargram, which serves as the input of CycleGAN, (b) the normlizaed permittivity profile, representing the true geological model used to generate the radaragram in (a) by running the gprMax open source code, (c) the inverted permittivity profile after applying the well-trained CycleGAN model, (d) smoothed permittivity profile of (c) using gaussian filters with sigma of (5, 10), (e) the residual map between the predicted permittivity profile (c) and the true permittivity profile (b), (f) the error histogram of (e), (g) normalized radar signal at trace #290, (h) normalized permittivity at trace #290, the blue solid line (Sim.) represents the synthetic geological model, the red solid line (CycleGAN) represents the predicted permittivity via CycleGAN and the green solid line (CNN) represents the predicted permittivity via CNN, (i) normalized radar signal at trace #82, (j) normalized permittivity at trace #82, the blue solid line (Sim.) represents the synthetic geological model, the red solid line (CycleGAN) represents the predicted permittivity via CycleGAN and the green solid line (CNN) represents the predicted permittivity via CNN.

3.4. Loss tangent and $FeO + TiO_2$ abundances

The loss tangent is a function of the bulk density (ρ) and the (TiO_2 + FeO) abundance (Li et al., 2020; Lai et al., 2020), which is defined as follows:

$$tan\sigma = 10^{(0.038(\%FeO+\%TiO_2)+0.312\rho-3.26))} \tag{7}$$

As indicated by (Li et al., 2020), the calculated average loss tangent is $(5 \pm 2) \times 10^{-3}$. Using the specific value of the loss tangent and bulk density (Fig. 9), the oxide content along the traversing path could be calculated based on the Eq. (7). Fig. 9 presents the $FeO + TiO_2$ abundance along the traversing path. According to the calculation results, the $FeO + TiO_2$ abundance is found to range from 1% to 8.5% using Olhoeft's density model (Fig. 8A), and it ranges from 1% to 12% using Hickson's density model (Figs. 8B). It is evident that the oxide contents in the lunar subsurface regolith reach 8.5% and 12%, which are consistent with previous research results (Li et al., 2020). This also demonstrates strong concordance with the orbital data values of 11% ∼ 16% for the VK crater (Ohtake et al., 2008), as determined by the Kaguya Multiband Imager data (Hickson et al., 2018).

4. Discussion

4.1. Reconstruction of the stratigraphic sequence

In this study, we initially examined the neighboring impact craters as depicted in Fig. 1A, focusing on their contribution to the ejecta at the Yutu-2 site and the relative formation times of these craters, as discussed by Xu et al. (2021) and Lu et al. (2021). According to Xu et al. (2021), a minimum of six impact craters with diameters exceeding 100km contributed at least 10 cm of ejecta to the CE-4 landing site. Furthermore, approximately ten smaller post-mare craters, including Finsen, Von Kármán L (VKL), Von Kármán L' (VKL'), and Antoniadi, with diameters less than 100 km, collectively contributed an estimated total ejecta thick-

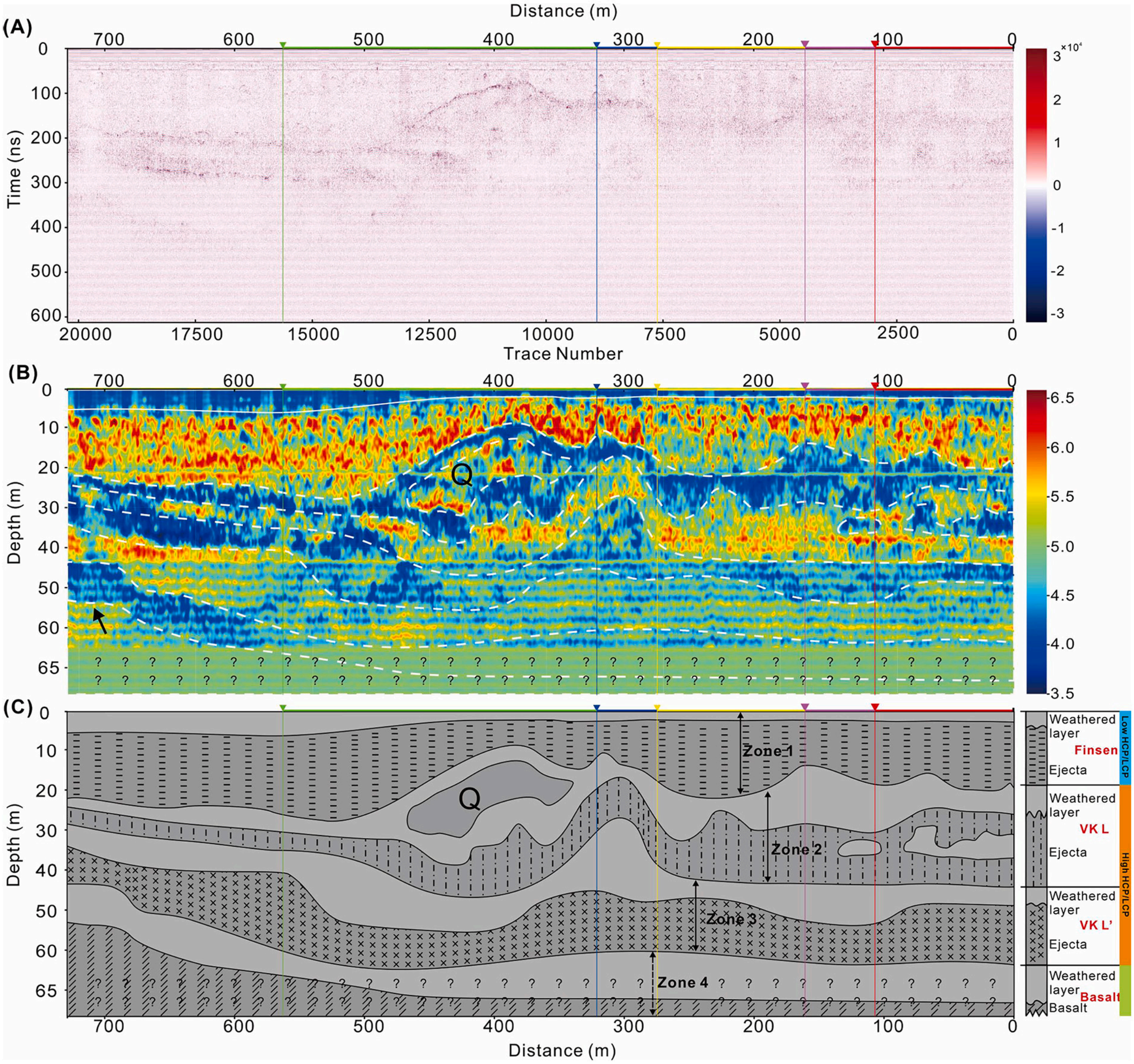

Fig. 6. LPR results and subsurface tomographic reconstruction of the Yutu-2 traversing path. (A) The radargram of CH2A is represented in a standard seismic color scheme and pre-processed based on the radar signal method proposed by Li et al. (2020). The x-axis represents the rover's distance (starting from the right), and the y-axis represents the two-way travel time. From right to left, five triangles with different colors mark the endpoints of different previous studies (Li et al., 2020; Zhang et al., 2021; Yuan et al., 2021; Zhang et al., 2020; Lai et al., 2021). It is notable that the radargram profile is a 2D profile, while the actual trajectory of the Yutu-2 rover traverse is twisted. (B) The permittivity profile inverted by CycleGAN along the rover traveling path in the depth domain. The red color indicates high dielectric permittivity, while cold colors indicate low dielectric permittivity. The interpreted interfaces are marked with white dashed lines, primarily based on the inverted permittivity values. (C) The proposed stratigraphic sequence highlights the difference between various zones and displays the relevant thickness based on the radargram (A) and the inverted permittivity profile (B).

ness of approximately ~ 17.1 meters to the CE-4 landing site. In this research, the most promising interpretation is that the ejecta from the Finsen ($3.1^{+0.3}_{-0.5}$ Ga), Von Kármán L (VKL), and Von Kármán L' (VKL') craters might be present on the floor of the Von Kármán crater (4.2 ± 0.03 Ga), overlaying the Imbrian-aged mare basalts. This is consistent with the proposed sequence by Fortezzo et al. (2020), as well as the thickness estimation of impact ejecta as discussed later. Furthermore, previous studies suggest the presence of ejecta from the Oriental Basin at the CE-4 site (Xiao et al., 2021). Various models have been utilized to estimate the age of the Oriental Basin, yielding distinct ranges such as approximately $\sim 3.68Ga$ (Whitten et al., 2011), $\sim 3.72Ga$ (Stoffler et al., 2006), $\sim 3.8Ga$ (Wilhelms and Byrne, 2009), and $3.92Ga$ (Werner et al., 2022). Despite the differences in these estimated ages, they all indicate that the ejecta from the Oriental Basin at the CE-4 site overlays the Imbrian-aged basalts.

As illustrated in Fig. 6A and B, the reconstructed stratigraphic sequence of the lunar subsurface does not demonstrate significant changes based on the radar reflection pattern and the inverted dielectric permittivity. Instead, smooth reflections between the layers exhibit vertical and horizontal variations. Based on the inverted permittivity profile (Fig. 6), four potential distinct zones were identified along the Yutu-2 site. Each of these zones is characterized by an upper low-permittivity layer and a lower high-permittivity layer (Fig. 6B).

The thickness of Zone 1 varies from east to west (from left to right), with an average thickness of approximately 18.8 meters. The thickness of the upper low-permittivity layer changes along the Yutu-2 traveling path, ranging from 1.5 ~ 6.7 meters, with an average thickness of 3.3 meters and an average dielectric permittivity of 3.94 for the upper low-permittivity regolith layer (Fig. 6C). Previous research (Huang et al., 2018; Yuan et al., 2021) suggests that CE-4 landed on the ejecta blanket of the Finsen crater due to its clear ejecta blanket extending from the

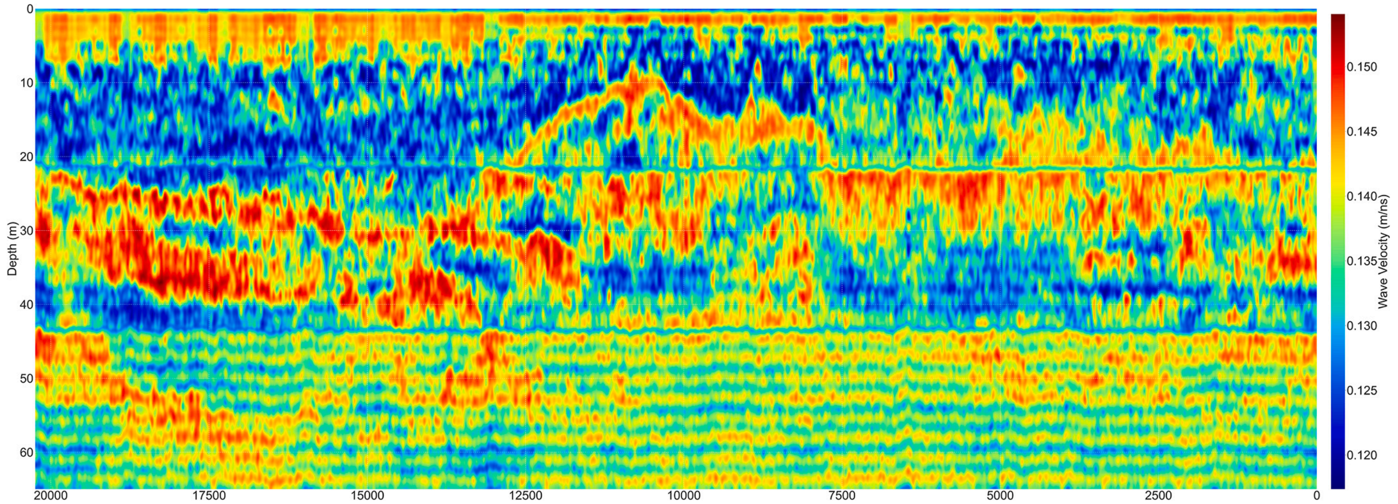

Fig. 7. Wave velocity profile. The velocity model presented herein is derived from the permittivity profile, as depicted in Fig. 6B, which has been inverted through the application of the CycleGAN algorithm. Furthermore, this velocity model is employed in the process of time-to-depth conversion, as illustrated in Fig. 6B.

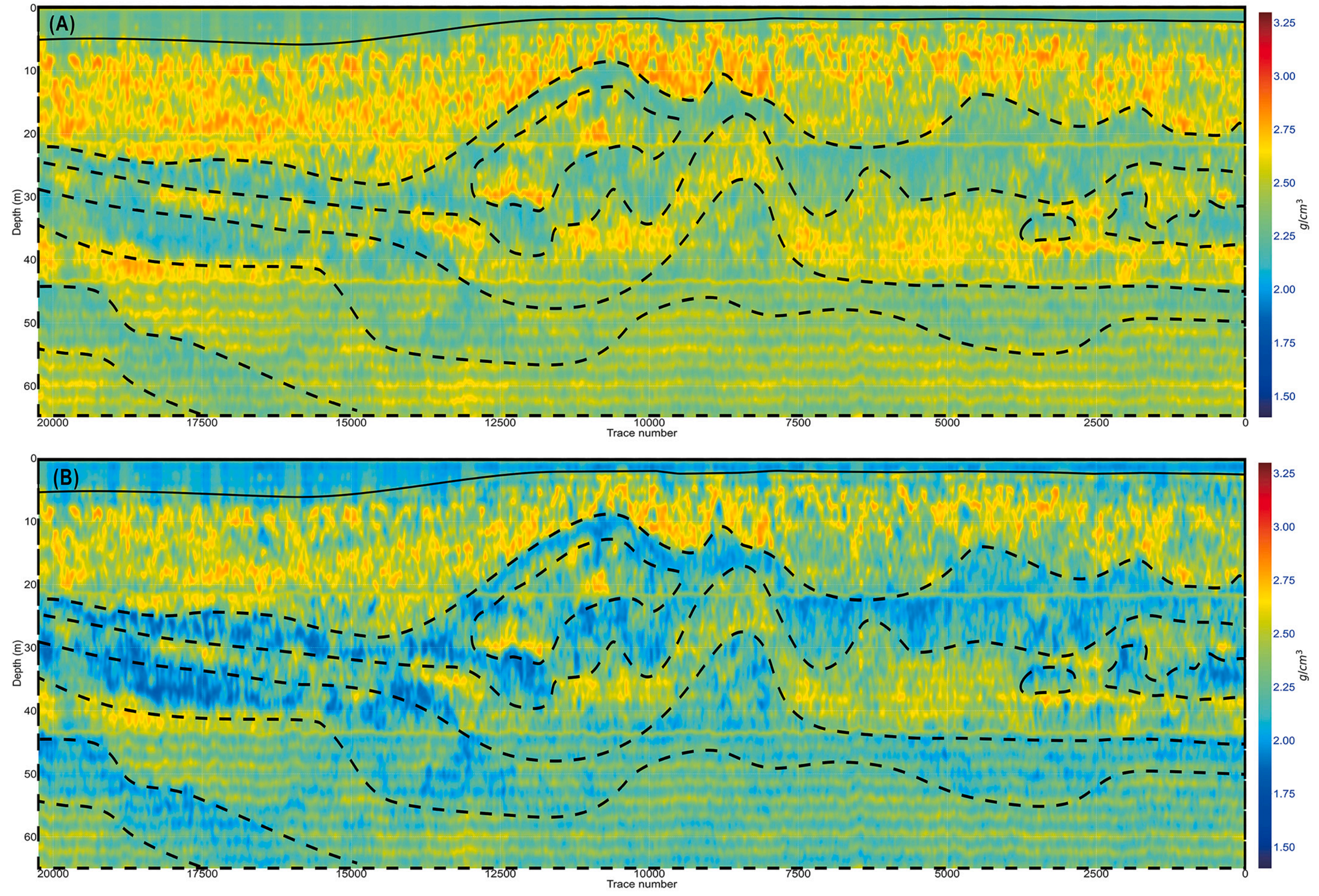

Fig. 8. Density profile. (A) The density profile is computed utilizing the formula suggested by Olhoeft and Strangway (1975), while (B) the density profile is determined through the application of the equation put forth by (Hickson et al., 2018).

northeast to the CE-4 site (Fig. 1A). It is proposed that the materials of subdivided Zone 1 are ejecta originating from the Finsen crater, with a thickness of 15.5 meters. Impact gardening increases porosity, resulting in a decrease in overall porosity, bulk density, and dielectric permittivity of multi-phase media (Dobson et al., 1985; Peplinski et al., 1995), and vitrification transforms lunar materials into glass fragments (Hörz et al., 1991; Nash and Conel, 1973). Therefore, the lunar regolith formed by weathering the ejecta is a low-permittivity medium, as demonstrated through laboratory (Carrier III et al., 1991), remote sensing (Gong et al., 2014; Bhattacharya et al., 2015), and in situ measurements (Dong et al., 2021). The permittivity of deeper layer ejecta is primarily estimated based on LPR measurements via a typical hyperbola-fitting algorithm

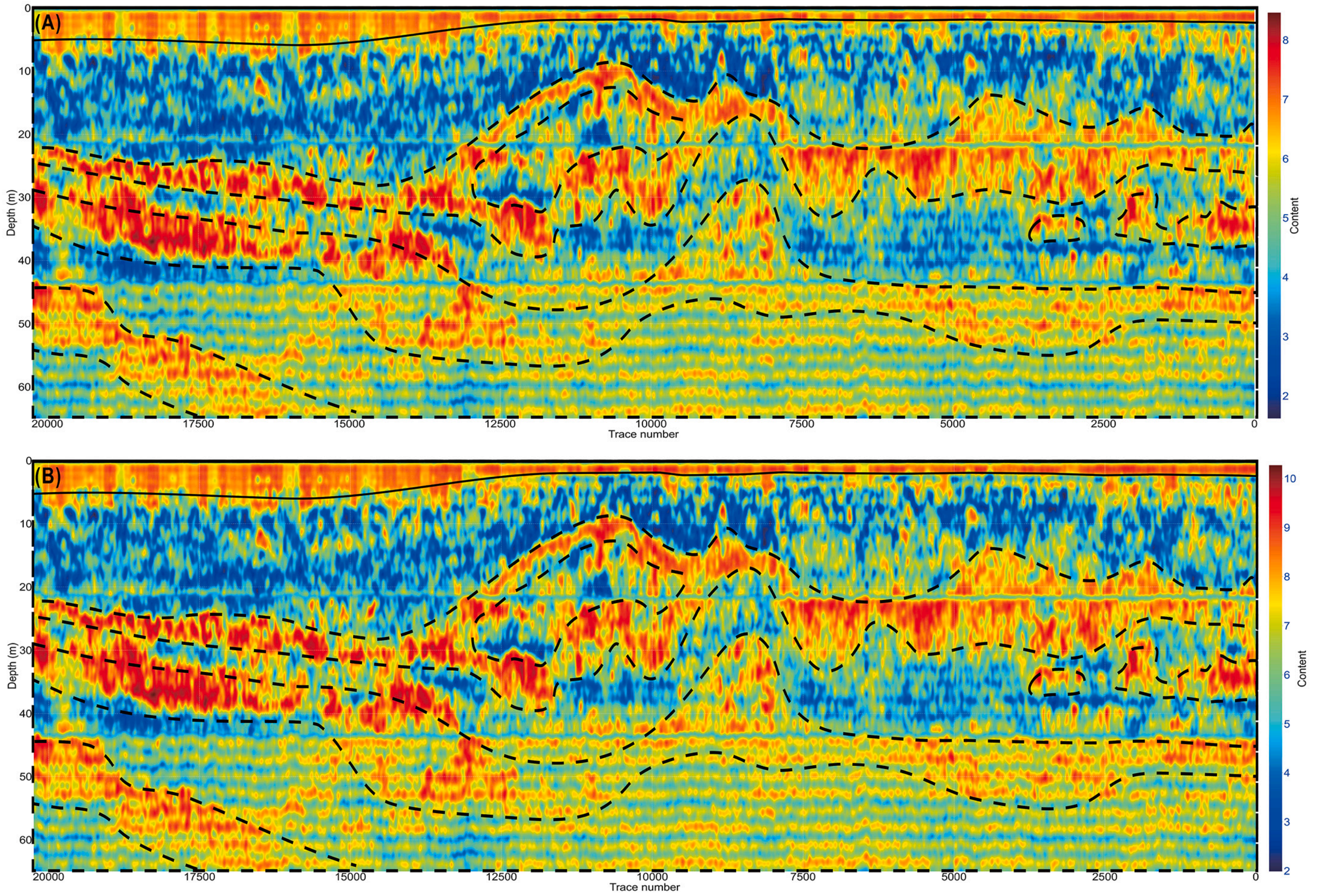

Fig. 9. $TiO + FeO_2$ abundance. (A) The oxide content calculated based on the equation proposed by Olhoeft and Strangway (1975); Li et al. (2020), and (B) the $TiO + FeO_2$ content calculated based on the equation proposed by (Hickson et al., 2018; Li et al., 2020).

(Dong et al., 2020; Zhang et al., 2022) or via the Complex Refractive Index Model (CRIM) (Birchak et al., 1974), with a bulk relative permittivity value as high as $\epsilon = 9$ (Giannakis et al., 2021). Therefore, the high-permittivity bottom layer might represent the more primitive ejecta, while the low-permittivity upper layer might represent the lunar soil formed by weathering the ejecta (Fig. 6). The estimated regolith thickness based on the crater morphology method at the Yutu-2 site is between $2.5 \sim 7.5$ meters (Huang et al., 2018), which agrees with the calculated upper low-permittivity layer thickness in this research ($1.5 \sim 6.7$ meters).

Zone 2, which extends from 19 meters to 38.5 meters from west to east, consists of a top low-permittivity layer with an average thickness of 9.4 meters and a bottom high-permittivity layer with an average thickness of 10.1 meters. As shown in Fig. 6B, the radar reflections in this zone are discontinuous, and the thickness decreases from east to west, which differs from Zone 1. The average thickness of this zone is approximately 19.5 meters. The permittivity estimated via CycleGAN in this research is 6.5, which is similar to the value of 6.8 estimated by Lai et al. (2021). Therefore, it is proposed that Zone 2 might contain ejecta from the VKL crater. Due to the gap between the formation of the Finsen and VKL craters, a low-permittivity paleo-regolith layer, might be formed by weathering, overlay on the high-permittivity paleo-regolith of the VKL crater. Additionally, a high-permittivity zone was discovered in the middle of the travel path, with inner low-permittivity materials, marked as "Q" in Fig. 6C. This location likely represents a buried crater with a diameter of 270 ± 10 meters and a radial gradient of 29°, as suggested by Lai et al. (2021). As indicated by Gornostaeva et al. (2019), the presence of a large number of glass fragments in the impact crater can lead to an increase in dielectric permittivity. This conclusion was reached through a detailed comparison of the composition and microstructure of terrestrial and lunar impact glass samples from the Zhamanshin crater and the Luna 16, 20, and 24 missions (Gornostaeva et al., 2019). These findings suggest that the abnormally high-permittivity geobody, marked as "Q" in Fig. 6C has high chance to be an impact crater. Furthermore, the newly discovered annulus feature and 2D scan radar characteristics also support that this location likely represents a buried crater with a diameter of 270 ± 10 meters and a radial gradient of 29° (Lai et al., 2021).

Zone 3, within the depth range of $39 \sim 59$ meters, exhibits the same pattern as Zone 1 and Zone 2, characterized by an upper low-permittivity layer with an average thickness of 8.5 meters and a bottom high-permittivity layer with an average thickness of 12.2 meters. It is suggested to interpret the Zone 3 as ejecta from the VKL' crater, formed before the VKL crater. The high-permittivity layer represents the primitive ejecta from VKL', while the upper low-permittivity layer is a paleo-regolith layer formed on the ejecta layer. This paleo-regolith layer developed potentially due to exposure to the harsh environment of space before the deposition of the VKL ejecta.

Zone 4, located below 60 meters, lacks a clear inner structure. An upper low-permittivity layer and a bottom high-permittivity layer develop in the eastern part of the rover's traveling path (indicated by the black arrow in Fig. 6C), similar to the patterns observed in Zones 1 to 3. However, for most parts of Zone 4, distinguishing the boundary between the high- and low-permittivity layers is challenging due to the fuzzy reflection characteristics. In particular, below 60 meters, the radar reflections are weak and diffuse. It is suggested to interpret the basal layer of this region as Imbrian-aged mare basalts (Fig. 6C). The upper low-permittivity layer is another paleo-regolith layer that developed on the lower high-permittivity basal mare basaltic layer, which formed approximately 3.2-3.3 Ga (Lu et al., 2021).

In summary, by combining information from the radargram (Fig. 6A), the inverted permittivity profile (Fig. 6B), calculated wave velocity (Fig. 7), estimated bulk density (Fig. 8), and estimated $TiO_2 + FeO$ abundance (Fig. 9), it is proposed that the CE-4 site in the VK crater has been modified by at least three major impact events following the deposition of Imbrian-aged mare basalts, resulting in at least four stratigraphic units (Fig. 6C). The upper low-permittivity layers of all four zones might be regolith (or paleo-regolith) produced by space weathering on the lower, more consolidated and rockier high-permittivity ejecta or basalt. These depositions are not continuous, exposing each lower layer to space for millions of years, allowing for regolith formation. Through a similar mechanism, the VKL' ejecta overlaps the regolith and primitive basalts in Zone 4; the VKL ejecta overlaps the regolith and primitive VKL' ejecta in Zone 3; and the Finsen ejecta overlaps the regolith and primitive VKL ejecta in Zone 2, following the formation of a localized 270 ± 10 meter crater that is now buried. Subsequently, no major impact events occurred around the VK crater, and the top regolith layer formed on the ejecta of the Finsen crater in Zone 1, which is currently being investigated by CE-4. Altogether, these four zones were stacked together to form layered deposits from the Imbrian period to the present, through similar mechanisms.

4.2. Comparison with previous studies

Based on the inverted permittivity profile (Fig. 6B) and calculated wave velocity (Fig. 8), the time-to-depth conversion in this study differs from previous studies, which use a constant wave velocity of 0.16 m/ns (Li et al., 2020). Therefore, most interpreted boundaries remain the same between in this research and previous works in the time domain, they differ significantly in the depth domain if the estimated wave velocity in this study is closer to the real case. Previous studies (Li et al., 2020; Zhang et al., 2020, 2021; Yuan et al., 2021) identified the top 12 meters to be lunar regolith due to its homogeneous and continuous reflection features. However, based on our inverted permittivity profile, the thickness of the regolith is estimated to be approximately 3.3 meters (the upper layer of Zone 1), which is more consistent with the results estimated via crater morphology method (Huang et al., 2018).

Fig. 10 displays the comparison between our research and Li's study Li et al. (2020). After comprehensively comparison, four zones were proposed in shallow subsurface (Fig. 10C and D), which is very similar to the three units interpreted by Li et al. (2020) (Fig. 10D). Unit 1 and Zone 1 share the same bottom boundary, while Unit 2 and Zone 2 have the same interpreted boundary, as marked by numbers ① and ② in Fig. 10D. The bottom of Unit 3 is higher than that of Zone 3 due to a change in permittivity value at this boundary. There are also several differences between the two studies. The numbers ③, ④, and ⑤ mark the values change at these points, which provide detailed interpretations for these points compared with previous research. Additionally, Li et al. (2020) suggested that there was a lens with fine-grained materials and no large rocks in Unit 3. However, few such special geological bodies were identified in this research because there is no significant permittivity change in these regions according to the inverted permittivity profile in this study (Fig. 6B).

Fig. S3 shows the comparison between this research and Zhang's study (Zhang et al., 2021). Zhang et al. (2021) posited that the top 34 meters consist of fine-grained regolith and multilayered ejecta emitted from the Finsen crater, with the top layer being fine-grained regolith and the bottom layer being ejecta from other craters. Though, the boundary of the first layer is consistent with the interpreted results in this study, the interpretation differs. We suggested that the first layer originates from the Finsen crater, whereas the bottom Zone 2 and Zone 3 are from the VKL and VKL' craters, respectively. The blue numbers ① to ⑤ mark boundaries consistent with Zhang's interpretation, while the red numbers ⑥ and ⑦ mark new interpreted boundaries in this research. Additionally, the purple numbers ⑧ and ⑨ indicate regions with no clear identification due to the fuzzy reflection signals.

Fig. S4 shows the comparison between this research and Yuan's study (Yuan et al., 2021). According to Yuan et al. (2021), the interfaces A, B, and B', marked by the black dashed lines in Fig. S4D, are consistent with our interpretation because Yuan's results included elevation correction, indicated by blue numbers ① to ⑤. However, the interface from C to $C4$ is inconsistent with our interpretation. Yuan et al. (2021) also identified several sub-interfaces, which are marked by green numbers ⑥ and ⑦. These sub-interfaces are consistent with our interpretation, where these signals are interpreted as the inner high-permittivity layer in Zone 2. Moreover, (Yuan et al., 2021) also interpreted the boundary of the buried crater, marked by purple numbers ⑧ and ⑨, as the inner-geological body boundary.

Fig. S5 shows the comparison between our research and Zhang's study (Zhang et al., 2020). According to Zhang (Zhang et al., 2020), several interfaces are similar to the interpreted interfaces in this study, marked by blue numbers ① to ⑩, but with different geological interpretations. The green letters a, b, and c mark possible sub-interfaces in our research, which are interpreted as layer boundaries in Zhang's study.

Fig. S6 shows the comparison between our research and Lai's study (Lai et al., 2021). The interpretation results for the first layer in Lai's study and our Zone 1 are consistent, as marked by blue numbers ① to ⑤. Green numbers ⑤ to ⑨ mark a special layer or interface shown in Lai's study. The purple letters a, b, and c indicate several clear property changes in Lai's study and are also consistent with our interpretation. The black rectangle highlights a complex region in Lai's study, where some faults are interpreted.

4.3. Crust-mantle material in the SPA basin

According to Wieczorek et al. (2013), the average densities of the lunar highland crust and mantle materials are 2.55 g/cm^3 and $3.15 \sim 3.37$ g/cm^3, respectively. Based on the estimated bulk density, the bulk density of Zone 1 ejected from the Finsen crater ranges from $2.25 \sim 3.25$ g/cm^3, and the bottom high-permittivity layer of Zone 1 has an bulk density of $2.81 \pm 0.22 g/cm^3$, which is denser than pure highland materials with a density of $2.55 g/cm^3$. The Finsen crater has a diameter of 73.1 km, with an approximate excavation depth of $3.7 \sim 4.8$ km ($H_{exc} \approx 0.05 \sim 0.065D$, where D is the final complex crater diameter) (Melosh et al., 2017). The Finsen crater may deliver the floor material of the SPA, which is widely thought to penetrate the upper lunar mantle (Potter et al., 2012; Melosh et al., 2017), to the CE-4 landing site. According to high-spectral and high-spatial-resolution Moon Mineralogy Mapper (M^3) data, the central peak of the Finsen crater exhibits mafic components likely from the uplifting of the lower crust or upper mantle within the transient cavity of the SPA (Moriarty et al., 2013). Therefor, if the estimated bulk densities in this research are correct, then a promising conclusion could be that the upper layers of ejecta in Zone 1 at the landing site were delivered by the Finsen impact, or at least the materials are mixed with a large portion of the lunar mantle, which could suggest the presence of mantle material consistent with impact models of SPA bringing olivine to the surface, as the higher end of density estimation for Zone 1 (2.81 ± 0.22 g/cm^3) is much greater than that of highland materials (2.55 g/cm^3) or basalts (2.6 g/cm^3) (Wilson and Head, 2017). Previous research has used visible near-infrared spectra to constrain the material properties investigated by Yutu-2 (Li et al., 2019; Lin et al., 2020; Huang et al., 2020), but significant disputes exist due to the poor understanding of the highly weathered top soil. Additionally, the high content of fragments at the bottom of Zone 1 may also contribute to the high bulk density and dielectric permittivity of this zone, which requires further investigation.

As previously proposed, the materials of Zone 2 and Zone 3 might be ejected from the VKL and VKL' craters, respectively. The VKL and VKL' craters have diameters of 29.6 km and 29.0 km, with excavation

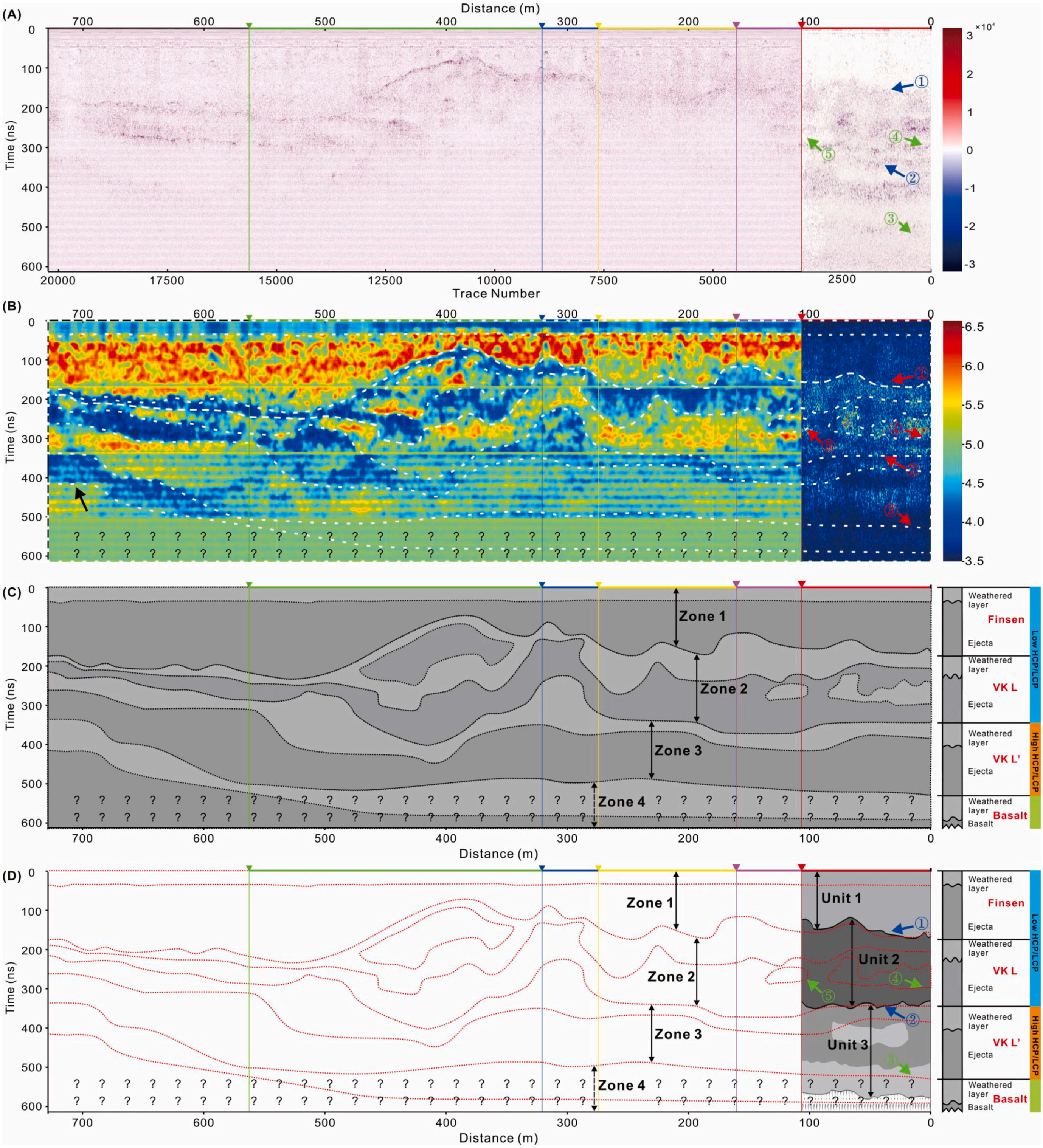

Fig. 10. The result comparison between Li's research Li et al. (2020). (A) the processed radargram in this research overlapped with Li's result in the same interval, marked by a red triangle. (B) the inverted permittivity by Cycle-GAN in this study and overlapped by Li's tomographic reconstruction result in the same interval in the time domain. (C) the proposed stratigraphic sequence framework in this study in the time domain. (D) the interpreted stratigraphic sequence framework overlapped by Li's interpretation (Li et al., 2020)(D).

depths of 1.5 ~ 1.9 and 1.45 ~ 1.89 km, respectively, based on previous research (Yuan et al., 2021). These excavation depths are much smaller than that of the Finsen crater (3.7 ~ 4.8 km), which means the materials excavated by the VKL and VKL' craters are likely shallower than those excavated by the Finsen crater. Additionally, the estimated bulk densities of Zone 2 and Zone 3, delivered from the VKL and VKL' craters, range from 2.0 ~ 2.75 g/cm^3, which is similar to those of highland materials. Therefore, if the estimated bulk density is accurate, it can be concluded that crustal materials were excavated and delivered to the CE-4 site from the smaller VKL and VKL' craters, while mantle materials were excavated and delivered to the floor of SPA from the larger Finsen crater.

According to the compositional subdivision of the SPA basin based on hyperspectral data (Moriarty Iii and Pieters, 2018), the Finsen crater is located in the SPA Compositional Anomaly (SPACA) area, while the VKL and VKL' craters are located in the Mg-Pyroxene Annulus area (Fig. 1A). Therefore, the impact targets of these three major ejecta source craters may be distinct. The Finsen, VKL, and VKL' craters serve as extraordinary probes into the subsurface composition of the SPA basin. Moreover, mantle materials from the Finsen crater can be excavated from the SPACA area, indicating that the SPA might exposed the lunar upper mantle, which is currently deposited in the SPACA area. In contrast, the targets of the VKL and VKL' craters, located in the Mg-Pyroxene Annulus, might be primarily composed of lunar crustal materials.

Data archival

The Chang'E-2 global digital orthophoto map (20 m/pixel) and Chang'E-4 Lunar Penetrating Radar data are available from the Lunar and Planetary Data Release System (https://moon.bao.ac.cn/ce5web/moonGisMap.search). LPR file IDs are given in the Supporting Information (Tables S2 & S4). The base image in Figure 1B is the Chang'E-4 Landing Site low-Sun controlled NAC mosaic (1.40 m/px), which is available at the LROC website (https://www.lroc.asu.edu/ and https://wms.lroc.asu.edu/lroc/view_rdr_product/NAC_DTM_CHANGE4_M1303619844_140CM). Additional gprMax simulation training and testing datasets are available from the corresponding author upon reasonable request because of their huge volume.

CRediT authorship contribution statement

Zhi Zhong: Writing – review & editing, Writing – original draft, Visualization, Validation, Software, Methodology, Funding acquisition, Data curation, Conceptualization. **Yuqi Qian:** Writing – review & editing, Writing – original draft, Conceptualization. **Chenglong Li:** Visualization, Validation, Methodology, Data curation. **Alexander Y. Sun:** Writing – review & editing, Writing – original draft, Resources, Methodology. **Zhongxian Cai:** Writing – original draft, Investigation, Funding acquisition. **Lei Lin:** Visualization, Validation, Methodology. **Xu Guo:** Data curation. **Yanbin Kuang:** Data curation. **Shiqi Wen:** Data curation. **Long Xiao:** Writing – review & editing, Supervision, Resources.

Declaration of competing interest

The authors declare that they have no known competing financial interests or personal relationships that could have appeared to influence the work reported in this paper.

The author is an Editorial Board Member/Editor-in-Chief/Associate Editor/Guest Editor for [*Earth and Planetary Science Letters*] and was not involved in the editorial review or the decision to publish this article.

Data availability

Data will be made available on request.

Acknowledgement

The authors declare the existence of a/non-financial competing interest. This study is supported by the National Natural Science Foundation of China (Grants No. 42202171) and the Key Research and Development Project of Hubei Province Technology Innovation Plan (Grants No. 2023BCB105). We sincerely thank the China National Space Administration (CNSA) for providing the LPR data, and the PaddlePaddle team (https://www.paddlepaddle.org.cn/) of Baidu for providing the arithmetic support in this study.

Appendix A. Supplementary material

Supplementary material related to this article can be found online at https://doi.org/10.1016/j.epsl.2024.118923.

References

Al-Nuaimy, W., Huang, Y., Nakhkash, M., Fang, M., Nguyen, V., Eriksen, A., 2000. Automatic detection of buried utilities and solid objects with gpr using neural networks and pattern recognition. J. Appl. Geophys. 43, 157–165.

Bhattacharya, A., Porwal, A., Dhingra, S., De, S., Venkataraman, G., 2015. Remote estimation of dielectric permittivity of lunar surface regolith using compact polarimetric synthetic aperture radar data. Adv. Space Res. 56, 2439–2448.

Birchak, J.R., Gardner, C.G., Hipp, J.E., Victor, J.M., 1974. High dielectric constant microwave probes for sensing soil moisture. Proc. IEEE 62, 93–98.

Carrier III, W.D., Olhoeft, G.R., Mendell, W., 1991. Physical properties of the lunar surface.

Cassata, W.S., Cohen, B.E., Mark, D.F., Trappitsch, R., Crow, C.A., Wimpenny, J., Lee, M.R., Smith, C.L., 2018. Chronology of martian breccia nwa 7034 and the formation of the martian crustal dichotomy. Sci. Adv. 4, eaap8306.

Ciampoli, L.B., Benedetto, A., Pajewski, L., Alani, A.M., Tosti, F., 2016. A comparison between different central frequencies of investigation in buried utility detection through gpr: a study case. In: 2016 16th International Conference on Ground Penetrating Radar (GPR), IEEE, pp. 1–4.

Comite, D., Galli, A., Lauro, S.E., Mattei, E., Pettinelli, E., 2015. Analysis of gpr early-time signal features for the evaluation of soil permittivity through numerical and experimental surveys. IEEE J. Sel. Top. Appl. Earth Obs. Remote Sens. 9, 178–187.

Di Matteo, A., Pettinelli, E., Slob, E., 2012. Early-time gpr signal attributes to estimate soil dielectric permittivity: a theoretical study. IEEE Trans. Geosci. Remote Sens. 51, 1643–1654.

Dobson, M.C., Ulaby, F.T., Hallikainen, M.T., El-Rayes, M.A., 1985. Microwave dielectric behavior of wet soil-part ii: dielectric mixing models. IEEE Trans. Geosci. Remote Sens., 35–46.

Dong, Z., Fang, G., Zhao, D., Zhou, B., Gao, Y., Ji, Y., 2020. Dielectric properties of lunar subsurface materials. Geophys. Res. Lett. 47, e2020GL089264.

Dong, Z., Fang, G., Zhou, B., Zhao, D., Gao, Y., Ji, Y., 2021. Properties of lunar regolith on the moon's farside unveiled by chang'e-4 lunar penetrating radar. J. Geophys. Res., Planets 126, e2020JE006564.

Fa, W., Zhu, M.H., Liu, T., Plescia, J.B., 2015. Regolith stratigraphy at the Chang'E-3 landing site as seen by lunar penetrating radar. Geophys. Res. Lett. 42.

Feng, Y., Chen, S., Tong, X., Wang, C., Li, P., Xi, M., Xiao, C., 2023. Exploring the lunar regolith's thickness and dielectric properties using band-limited impedance at chang'e-4 landing site. J. Geophys. Res., Planets 128, e2022JE007540.

Fernandes, V., Fritz, J., Weiss, B., Garrick-Bethell, I., Shuster, D., 2013. The bombardment history of the moon as recorded by 40ar-39ar chronology. Meteorit. Planet. Sci. 48, 241–269.

Fortezzo, C., Spudis, P., Harrel, S., 2020. Release of the digital unified global geologic map of the moon at 1: 5,000,000-scale. In: 51st Annual Lunar and Planetary Science Conference, p. 2760.

Gao, K., Donahue, C., Henderson, B.G., Modrak, R.T., 2023. Deep-learning-guided high-resolution subsurface reflectivity imaging with application to ground-penetrating radar data. Geophys. J. Int. 233, 448–471.

Garrick-Bethell, I., Miljković, K., Hiesinger, H., van der Bogert, C.H., Laneuville, M., Shuster, D.L., Korycansky, D.G., 2020. Troctolite 76535: a sample of the moon's South Pole-Aitken basin? Icarus 338, 113430.

Garrick-Bethell, I., Nimmo, F., Wieczorek, M.A., 2010. Structure and formation of the lunar farside highlands. Science 330, 949–951.

Giannakis, I., Giannopoulos, A., Warren, C., 2016. A realistic FDTD numerical modeling framework of ground penetrating radar for landmine detection. IEEE J. Sel. Top. Appl. Earth Obs. Remote Sens. 9, 37–51.

Giannakis, I., Zhou, F., Warren, C., Giannopoulos, A., 2021. Inferring the shallow layered structure at the chang'e-4 landing site: a novel interpretation approach using lunar penetrating radar. Geophys. Res. Lett. 48, e2021GL092866.

Gong, X., Paige, D.A., Siegler, M.A., Jin, Y.Q., 2014. Inversion of dielectric properties of the lunar regolith media with temperature profiles using chang'e microwave radiometer observations. IEEE Geosci. Remote Sens. Lett. 12, 384–388.

Goodfellow, I., Pouget-Abadie, J., Mirza, M., Xu, B., Warde-Farley, D., Ozair, S., Courville, A., Bengio, Y., 2014. Generative adversarial nets. Adv. Neural Inf. Process. Syst. 27.

Goodfellow, I., Pouget-Abadie, J., Mirza, M., Xu, B., Warde-Farley, D., Ozair, S., Courville, A., Bengio, Y., 2020. Generative adversarial networks. Commun. ACM 63, 139–144. https://doi.org/10.1145/3422622.

Goodfellow, I.J., Vinyals, O., Saxe, A.M., 2015. Qualitatively characterizing neural network optimization problems.

Gornostaeva, T., Mokhov, A., Kartashov, P., Bogatikov, O., 2019. Comparison of the compositions and microstructures of terrestrial and lunar impact glasses: samples from the Zhamanshin crater and Luna 16, 20, and 24 missions. Petrology 27, 95–107.

Hickson, D., Boivin, A., Daly, M.G., Ghent, R., Nolan, M.C., Tait, K., Cunje, A., Tsai, C.A., 2018. Near surface bulk density estimates of neas from radar observations and permittivity measurements of powdered geologic material. Icarus 306, 16–24.

Hörz, F., Grieve, R., Heiken, G., Spudis, P., Binder, A., 1991. Lunar surface processes.

Huang, J., Xiao, Z., Flahaut, J., Martinot, M., Head, J., Xiao, X., Xie, M., Xiao, L., 2018. Geological characteristics of von Kármán crater, northwestern South Pole-Aitken basin: chang'e-4 landing site region. J. Geophys. Res., Planets 123, 1684–1700.

Huang, J., Xiao, Z., Xiao, L., Horgan, B., Hu, X., Lucey, P., Xiao, X., Zhao, S., Qian, Y., Zhang, H., et al., 2020. Diverse rock types detected in the lunar South Pole–Aitken basin by the chang'e-4 lunar mission. Geology 48, 723–727.

Jolliff, B.L., Gillis, J.J., Haskin, L.A., Korotev, R.L., Wieczorek, M.A., 2000. Major lunar crustal terranes: surface expressions and crust-mantle origins. J. Geophys. Res., Planets 105, 4197–4216.

Koyama, C.N., Liu, H., Takahashi, K., Shimada, M., Watanabe, M., Khuut, T., Sato, M., 2017. In-situ measurement of soil permittivity at various depths for the calibration and validation of low-frequency sar soil moisture models by using gpr. Remote Sens. 9, 580.

Koyan, P., Tronicke, J., 2020. 3D modeling of ground-penetrating radar data across a realistic sedimentary model. Comput. Geosci. 137, 104422.

Lai, J., Xu, Y., Bugiolacchi, R., Meng, X., Xiao, L., Xie, M., Liu, B., Di, K., Zhang, X., Zhou, B., et al., 2020. First look by the yutu-2 rover at the deep subsurface structure at the lunar farside. Nat. Commun. 11, 1–9.

Lai, J., Xu, Y., Bugiolacchi, R., Wong, H.K., Xu, L., Zhang, X., Zhang, L., Zhang, X., Xiao, L., Liu, B., et al., 2021. A complex paleo-surface revealed by the yutu-2 rover at the lunar farside. Geophys. Res. Lett. 48, e2021GL095133.

LeCun, Y., Huang, F.J., Bottou, L., 2004. Learning methods for generic object recognition with invariance to pose and lighting. In: Proceedings of the 2004 IEEE Computer Society Conference on Computer Vision and Pattern Recognition. CVPR 2004. IEEE. pp. II–104.

Li, C., Liu, D., Liu, B., Ren, X., Liu, J., He, Z., Zuo, W., Zeng, X., Xu, R., Tan, X., et al., 2019. Chang'e-4 initial spectroscopic identification of lunar far-side mantle-derived materials. Nature 569, 378–382.

Li, C., Su, Y., Pettinelli, E., Xing, S., Ding, C., Liu, J., Ren, X., Lauro, S.E., Soldovieri, F., Zeng, X., et al., 2020. The moon's farside shallow subsurface structure unveiled by chang'e-4 lunar penetrating radar. Sci. Adv. 6, eaay6898.

Lin, H., He, Z., Yang, W., Lin, Y., Xu, R., Zhang, C., Zhu, M.H., Chang, R., Zhang, J., Li, C., et al., 2020. Olivine-norite rock detected by the lunar rover yutu-2 likely crystallized from the spa-impact melt pool. Nat. Sci. Rev. 7, 913–920.

Lin, Y., Tronche, E.J., Steenstra, E.S., van Westrenen, W., 2017. Evidence for an early wet moon from experimental crystallization of the lunar magma ocean. Nat. Geosci. 10, 14–18.

Liu, J., Ren, X., Yan, W., Li, C., Zhang, H., Jia, Y., Zeng, X., Chen, W., Gao, X., Liu, D., et al., 2019. Descent trajectory reconstruction and landing site positioning of chang'e-4 on the lunar farside. Nat. Commun. 10, 1–10.

Lu, Y., Wu, Y., Michael, G.G., Ma, J., Cai, W., Qin, N., 2021. Chronological sequence of chang'e-4 landing zone within von Kármán crater. Icarus 354, 114086.

Melosh, H., Kendall, J., Horgan, B., Johnson, B., Bowling, T., Lucey, P., Taylor, G., 2017. South Pole–Aitken basin ejecta reveal the moon's upper mantle. Geology 45, 1063–1066.

Metwaly, M., 2015. Application of gpr technique for subsurface utility mapping: a case study from urban area of holy mecca, Saudi Arabia. Measurement 60, 139–145.

Moriarty, D., Pieters, C., Isaacson, P., 2013. Compositional heterogeneity of central peaks within the South Pole-Aitken basin. J. Geophys. Res., Planets 118, 2310–2322.

Moriarty Iii, D., Pieters, C., 2018. The character of South Pole-Aitken basin: patterns of surface and subsurface composition. J. Geophys. Res., Planets 123, 729–747.

Moriarty III, D., Watkins, R., Valencia, S., Kendall, J., Evans, A., Dygert, N., Petro, N., 2021. Evidence for a stratified upper mantle preserved within the South Pole-Aitken basin. J. Geophys. Res., Planets 126, e2020JE006589.

Muhleman, D., Brown Jr, W., Davids, L., Negus, J., Peake, W., 1969. Lunar surface electromagnetic properties. NASA 184, 203–269.

Nash, D.B., Conel, J.E., 1973. Vitrification darkening of rock powders: implications for optical properties of the lunar surface. Moon 8, 346–364.

Neumann, G.A., Zuber, M.T., Wieczorek, M.A., Head, J.W., Baker, D.M., Solomon, S.C., Smith, D.E., Lemoine, F.G., Mazarico, E., Sabaka, T.J., et al., 2015. Lunar impact basins revealed by gravity recovery and interior laboratory measurements. Sci. Adv. 1, e1500852.

Ohtake, M., Haruyama, J., Matsunaga, T., Yokota, Y., Morota, T., Honda, C., 2008. Performance and scientific objectives of the selene (kaguya) multiband imager. Earth Planets Space 60, 257–264.

Olhoeft, G.R., Strangway, D., 1975. Dielectric properties of the first 100 meters of the moon. Earth Planet. Sci. Lett. 24, 394–404.

Otter, D.W., Medina, J.R., Kalita, J.K., 2020. A survey of the usages of deep learning for natural language processing. IEEE Trans. Neural Netw. Learn. Syst. 32, 604–624.

Pasckert, J.H., Hiesinger, H., van der Bogert, C.H., 2018. Lunar farside volcanism in and around the South Pole–Aitken basin. Icarus 299, 538–562.

Peplinski, N.R., Ulaby, F.T., Dobson, M.C., 1995. Dielectric properties of soils in the 0.3-1.3-ghz range. IEEE Trans. Geosci. Remote Sens. 33, 803–807.

Peters, L., Daniels, J.J., Young, J.D., 1994. Ground penetrating radar as a subsurface environmental sensing tool. Proc. IEEE 82, 1802–1822.

Potter, R.W., Collins, G.S., Kiefer, W.S., McGovern, P.J., Kring, D.A., 2012. Constraining the size of the South Pole-Aitken basin impact. Icarus 220, 730–743.

Qin, T., Bohlen, T., Allroggen, N., 2023. Full-waveform inversion of ground-penetrating radar data in frequency-dependent media involving permittivity attenuation. Geophys. J. Int. 232, 504–522.

Raissi, M., Karniadakis, G.E., 2018. Hidden physics models: machine learning of nonlinear partial differential equations. J. Comput. Phys. 357, 125–141.

Rehman, F., Abouelnaga, H.S.O., Rehman, F., 2016. Estimation of dielectric permittivity, water content, and porosity for environmental engineering and hydrogeological studies using ground penetrating radar, a short review. Arab. J. Geosci. 9, 1–7.

Sandmeier, K., 2023. Program for processing of seismic, acoustic or electromagnetic reflection, refraction and transmission data. In: Software Manual, pp. 1–628.

Stoffler, D., Ryder, G., Ivanov, B.A., Artemieva, N.A., Cintala, M.J., Grieve, R.A., 2006. Cratering history and lunar chronology. Rev. Mineral. Geochem. 60, 519–596.

Wang, H., Ouyang, S., Liu, Q., Liao, K., Zhou, L., 2022. Deep-learning-based method for estimating permittivity of ground-penetrating radar targets. Remote Sens. 14, 4293.

Warren, C., Giannopoulos, A., Giannakis, I., 2016. gprmax: open source software to simulate electromagnetic wave propagation for ground penetrating radar. Comput. Phys. Commun. 209, 163–170.

Warren, C., Giannopoulos, A., Gray, A., Giannakis, I., Patterson, A., Wetter, L., Hamrah, A., 2019. A CUDA-based GPU engine for gprMax: open source FDTD electromagnetic simulation software. Comput. Phys. Commun. 237, 208–218.

Warren, P.H.a., 1985. The magma ocean concept and lunar evolution. Annu. Rev. Earth Planet. Sci. 13, 201–240.

Werner, S.C., Bultel, B., Rolf, T., Fernandes, V.A., 2022. Orientale ejecta at the apollo 14 landing site implies a 200-million-year stratigraphic time shift on the moon. Planet. Sci. J. 3, 65.

Whitten, J., Head, J.W., Staid, M., Pieters, C.M., Mustard, J., Clark, R., Nettles, J., Klima, R.L., Taylor, L., 2011. Lunar mare deposits associated with the orientale impact basin: new insights into mineralogy, history, mode of emplacement, and relation to orientale basin evolution from moon mineralogy mapper (m3) data from chandrayaan-1. J. Geophys. Res., Planets 116.

Wieczorek, M.A., Neumann, G.A., Nimmo, F., Kiefer, W.S., Taylor, G.J., Melosh, H.J., Phillips, R.J., Solomon, S.C., Andrews-Hanna, J.C., Asmar, S.W., et al., 2013. The crust of the moon as seen by grail. Science 339, 671–675.

Wilhelms, D., Byrne, C., 2009. Stratigraphy of lunar craters. Image again online: http://www.imageagain.com/Strata/StratigraphyCraters2.

Wilson, L., Head, J.W., 2017. Generation, ascent and eruption of magma on the moon: new insights into source depths, magma supply, intrusions and effusive/explosive eruptions (part 1: theory). Icarus 283, 146–175.

Wu, W., Li, C., Zuo, W., Zhang, H., Liu, J., Wen, W., Su, Y., Ren, X., Yan, J., Yu, D., et al., 2019. Lunar farside to be explored by chang'e-4. Nat. Geosci. 12, 222–223.

Xiao, Z., Ding, C., Xie, M., Cai, Y., Cui, J., Zhang, K., Wang, J., 2021. Ejecta from the orientale basin at the chang'e-4 landing site. Geophys. Res. Lett. 48, e2020GL090935.

Xu, L., Zhang, X., Qiao, L., Lai, J., 2021. Evaluating the thickness and stratigraphy of ejecta materials at the chang'e-4 landing site. Astron. J. 162, 29.

Yamamoto, S., Nakamura, R., Matsunaga, T., Ogawa, Y., Ishihara, Y., Morota, T., Hirata, N., Ohtake, M., Hiroi, T., Yokota, Y., et al., 2012. Olivine-rich exposures in the South Pole-Aitken basin. Icarus 218, 331–344.

Yuan, Y., Zhu, P., Xiao, L., Huang, J., Garnero, E.J., Deng, J., Wang, F., Qian, Y., Zhao, N., Wang, W., et al., 2021. Intermittent volcanic activity detected in the von Kármán crater on the farside of the moon. Earth Planet. Sci. Lett. 569, 117062.

Zhang, J., Zhou, B., Lin, Y., Zhu, M.H., Song, H., Dong, Z., Gao, Y., Di, K., Yang, W., Lin, H., et al., 2021. Lunar regolith and substructure at chang'e-4 landing site in South Pole–Aitken basin. Nat. Astron. 5, 25–30.

Zhang, L., Li, J., Zeng, Z., Xu, Y., Liu, C., Chen, S., 2020. Stratigraphy of the von Kármán crater based on chang'e-4 lunar penetrating radar data. Geophys. Res. Lett. 47, e2020GL088680.

Zhang, N., Ding, M., Zhu, M.H., Li, H., Li, H., Yue, Z., 2022. Lunar compositional asymmetry explained by mantle overturn following the South Pole–Aitken impact. Nat. Geosci. 15, 37–41.

Zhong, Z., Sun, A.Y., Wu, X., 2020. Inversion of time-lapse seismic reservoir monitoring data using CycleGAN: a deep learning-based approach for estimating dynamic reservoir property changes. J. Geophys. Res., Solid Earth 125.

Zhou, H., Feng, X., Ding, C., Dong, Z., Liu, C., Liang, W., 2022. Heterogeneous weathering process of lunar regolith revealed by polarimetric attributes analysis of chang'e-4 lunar penetrating radar data acquired during the yutu-2 turnings. Geophys. Res. Lett. 49, e2022GL099207.

Zhu, J.Y., Park, T., Isola, P., Efros, A.A., 2017. Unpaired image-to-image translation using cycle-consistent adversarial networks, pp. 2223–2232.

Panda, S.L., Maiti, S., Sahoo, U.K., 2022. Subsurface propagation velocity estimation methods in ground-penetrating radar: a review. IEEE Geosci. Remote Sens. Mag. 10, 70–89.

Zhi Zhong received a B.S. in 2012 from the Chinese University of Geosciences (Wuhan) and a Ph.D. in 2017 from West Virginia University. He was a postdoctoral scholar in the Chemical and Petroleum Engineering Department at the University of Kansas from 2017 to 2018 and a postdoctoral scholar at the Bureau of Economic Geology (UT at Austin) from 2018-2020. Currently, he is a young research scientist at China University of Geosciences (Wuhan) since 2020. His current interests include seismic signal processing, numerical simulation, and machine learning.